MARCHE POLYTECHNIC UNIVERSITY

DEPARTMENT OF INFORMATION ENGINEERING

Master of Science in Biomedical Engineering

Reduction of laser fluctuations in real time optoacoustic volumetric mouse neuroimaging

Advisor:

Prof. **Lorenzo Scalise**

Coadvisors**:**

Dr. **Héctor Estrada**

Prof. **Simone Fiori**

Candidate:

Emilia Occhiodori

A.Y. 2020 / 2021

UNIVERSITÀ
POLITECNICA
DELLE MARCHE

Department of Information Engineering (DII)

Master of Science in Biomedical Engineering

Reduction of laser fluctuations in real time optoacoustic volumetric mouse neuroimaging

Advisor:

Prof. Lorenzo Scalise

Candidate:

Emilia Occhiodori

Coadvisors:

Dr. Héctor Estrada (ETH Zürich)

Prof. Simone Fiori

Academic Year 2020/2021

Università Politecnica delle Marche
Department of Information Engineering (DII)
Master of Science in Biomedical Engineering
Via Brecce Bianche – 60131 Ancona (AN), Italy

Abstract

The brain represents one of the less known yet most studied organs of the body. Scientists use imaging devices to better understand how the brain works, pursuing the hope of understanding and explaining the coupling mechanisms behind healthy structures and principles of neural dysfunctions.

Among various techniques currently used for neuroimaging, optoacoustic (OA) imaging emerges as a promising hybrid modality imaging system that allows non-invasive visualization and 5D investigation of biological structures. This technology combines high sensitivity and specificity of selective light absorption from tissues, with low scattering typical of ultrasound waves, which results in an imaging tool able of achieving optical contrast with the high ultrasonic resolution for imaging depth.

However, despite the promising abilities, OA appears to be non-immune to some limitations. In particular, the technique strongly relies on short laser-emitted light pulses to illuminate the target, which causes non-uniform light exposure and fluctuations of the illumination pattern both in time and space. In biological terms, variations in the light source would hamper the correct monitoring of slight changes in neuronal activity, hindering ongoing processes or enhancing unreal changes.

The work proposed in this thesis aims to investigate the optical nature of OAI, tackling the light fluctuations from a hardware and software perspective to reduce the alterations and obtain a more homogeneous and stable illumination pattern at the target interface.

At first, characterization of the laser beam has been performed, analyzing the variations both at the input and target interface through a camera and computation of statistical parameters. Then, the results for the original setup have been compared

with the ones relative to corrective hardware implementations, such as additional water filtering methods and optical corrections, evaluating the fluctuations variations and the temporal correlation over the batch of acquisition.

Afterward, the same hardware corrections have been implemented and tested on the full OAI system. The first test has been conducted imaging homogeneous phantoms, to test the efficiency of the hardware optimizations. Furthermore, given the multispectral nature of the acquired information, also software correction employing frame averaging has been implemented and compared to single frame reconstructions.

Eventually, pre-clinical in vivo OA neuroimaging has been performed to evaluate the results achieved through the proposed corrections.

The optimizations tested within this project proved to be valid allies in the assembly of the OA neuroimaging setup. In particular, water filtering and degassing allow preventing nuisance due to spurious signals generation and system deterioration. In this way, it is possible to reduce the spatial fluctuations present in the light distribution at the target interface, as proved by the strong temporal correlation present among different ROIs randomly selected in the illumination surface.
When employed in preclinical applications, that would improve the reliability of imaging of superficial structures, to which the photons are delivered with very little previous scattering.

Software correction tested on multispectral OA data proved to be able to reduce the temporal presence of artifacts and random noises, without losing the information related to ongoing hemodynamic changes.

To achieve a more stable control on temporal fluctuations, future works could focus on the investigation of temporal correlation among different voxels in raw or reconstructed OA data. Thus, identifying related regions, it would be possible to correct for the temporal variations affecting biologically informative voxels.

Table of Contents

List of Acronyms and Abbreviations

ADC	Analog to Digital Converter
BOLD	Blood Oxygenation Level-Dependent
CBF	Cerebral Blood Flow
CBV	Cerebral Blood Volume
DAQ	Data Acquisition system
EEG	Electroencephalography
fMRI	functional Magnetic Resonance Imaging
fUS	functional UltraSound
GPU	Graphics Processing Unit
HbO	Oxyhemoglobin
HbR	Deoxyhemoglobin
HbT	Total Hemoglobin
LNA	Low Noise Amplifier
MEG	Magnetoencephalography
MIPs	Maximum Intensity Projections
MM	Multi-Mode
MSOT	Multi Spectral OptoAcoustic Tomography
NIR	Near Infrared Range
O_2	Oxygen
OA	OptoAcoustic
OAI	OptoAcoustic Imaging
OAT	OptoAcoustic Tomography
PRF	Pulse Repetition Frequency

PD	Power Doppler
ROI	Region of Interest
SM	Single-Mode
SoS	Speed of Sound
std	standard deviation
US	UltraSound
USD	UltraSound Detectors
VIS	VISible

List of Figures

List of Tables

Chapter 1

Introduction

Synopsis In this first Chapter, Section 1.1 presents an overview of current techniques for brain visualization, stating their main advantages and disadvantages.
Section 1.2 illustrates a focus on OA neuroimaging.
Then, Section 1.3 presents the aim of the thesis, carried out at the laboratory of the *Multi-Scale Functional and Molecular Imaging group* of Prof. Dr. Daniel Razansky, at ETH and University of Zürich.
Eventually, Section 1.4 explains the outline of the thesis.

1.1 State of the art of neuroimaging modalities

The brain represents one of the less known yet most studied organs of the human body. It is well known that scientific knowledge is not able to explain nor fully understand the mechanisms during thinking and performing of actions. Being able to visualize in real-time and with an adequate level of detail what happens at the cerebral level would definitely help unravel the mysteries of brain functioning, as well as detect signs of emerging diseases [1, 2].

Neuroscientists have stated that correctly visualizing hemodynamic changes would allow a better understanding of the physiological activity of neurons [3]: in fact, it is known that changes in the blood flux are directly reflecting changes in the neural coupling, since brain areas activated by a specific task utilize more oxygen than the surrounding regions. Initially, such neural activation causes a decrease of the level of oxyhemoglobin (HbO) in the vasculature of the activated area, increasing levels of deoxyhemoglobin (HbR). Within seconds, however, the brain microvasculature

responds to the local deficiency of oxygen by increasing the flow of oxygen-rich blood to the activated area, to provide the necessary oxygen supply to the working tissues.

Hence, generically, by stimulating different areas of the body it is possible to detect a change in the activation of the correspondent brain area; furthermore, by evaluating the blood flux variations in the target brain area it is possible to monitor the health of the subject, as well as possibly early detect the presence of neurodegenerative diseases such as Alzheimer.

However, state of the art of available techniques to perform functional neuroimaging, report some limitations.

The gold standard is currently identified in functional magnetic resonance imaging (fMRI), a variation of MRI which provides 3D information about the brain activity [4, 5]. It can differentiate oxygenated hemoglobin from the deoxygenated one thanks to the different magnetic resonance signals originated by the two types of blood: oxyhemoglobin shows a diamagnetic property which does not affect the magnetic field, while deoxyhemoglobin is characterized by a paramagnetic nature, hence changes in its quantity causes changes in the resulting MR signal. These localized blood oxygenation level-dependent (BOLD) changes thus provide a contrast mechanism for detecting neuronal activity with fMRI (Figure 1.1). It should also be noted that BOLD fMRI does not directly measure neuronal activity, rather it measures the metabolic demand of the active ones, described by the hemodynamic response function (HRF), representing, precisely, changes in the fMRI signals triggered by the neuronal activity.

The main advantages of fMRI are its non-invasiveness and its high spatial resolution, which reaches a few mm levels. In addition, fMRI remains the main tool to investigate cognitive processes or psychiatric disorders given its ability to visualize the entire human brain, both rendering deeper cerebral structures and large-scale images [2].

Per contra, also several disadvantages may be listed. First of all the low temporal resolution, which is in the order of seconds hence not fast enough to faithfully map brain responses to single events [6]. In addition, while sufficient for mapping macro brain anatomy and activity, the mm-level spatial resolution must be judged according to the imaging purpose, as, for example, it is not able to resolve microvasculature

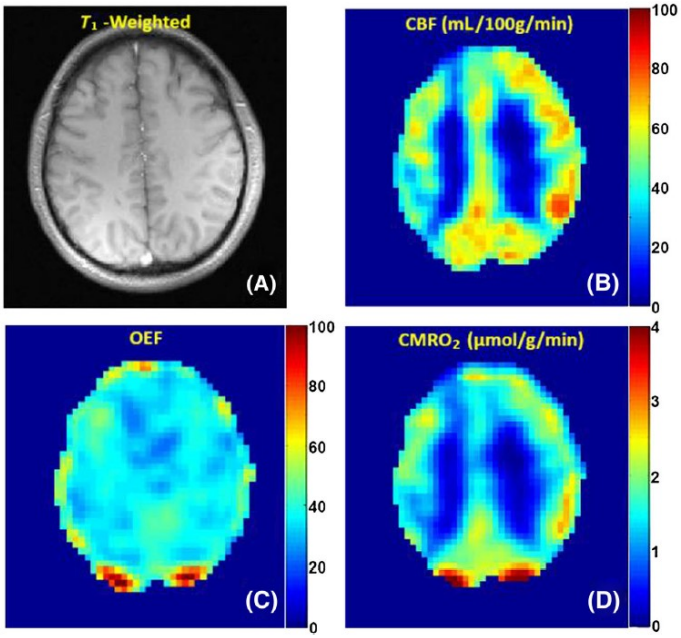

Figure 1.1: fMRI scans of the brain showing quantification of the cerebral metabolic rate of oxygen consumption ($CMRO_2$) in healthy subjects. (A) shows a high-resolution T1-weighted anatomic scan useful for comparison; (B) mapping of cerebral blood flow (CBF); (C) mapping of the oxygen extraction fraction (OEF); (D) map of ($CMRO_2$). (C) shows a quite homogeneus response in the brain, while in (B) and (D) are highlighted differences between gray matter and white matter [5].

[3]. Also, fMRI is suitable for a selective part of the population: due to the strong magnetic field generated by the machine (around 7T), no metal-based equipment can be allowed in the same room, thus preventing imaging of subjects with permanent ferromagnetic implants (pacemaker, prosthesis) or suffering from claustrophobia [7]. Eventually, also the ratio cost-benefit must be taken into account, and fMRI machines themselves are very expensive, not portable, and actually quite noisy [8, 9].

Additional methods are commonly performed for brain research purposes: however, either are they only able to satisfy temporal resolution conditions and lack in terms of spatial resolution and ability to provide anatomical information, such as MEG, EEG, and functional NIR spectroscopy [10, 11], or rely on the use of radioactive atoms, such as in nuclear-based techniques [12].

In order to overcome the current limitations of cerebral investigation approaches, other competing techniques are being improved in preclinical studies, to achieve a

more reliable and accurate neuroimaging methodology.

A branch of imaging methods that are arousing interest for in vivo neurovisualization is based on optical methods [13, 14]. These are mainly sensitive to O_2 level in the blood, hence capable of accurately differentiating between HbO and HbR.
However, the main limitation of optical methods is the limited imaging depth. The effects of intense photon scattering allow faithful brain structures visualization only at the superficial level, hindering deeper cerebral structures due to a substantial loss of spatial resolution [15, 16]. A certain level of invasiveness is also sometimes requested, in the form of scalp removal or skull thinning [15].

Recent studies performed functional neuroimaging through the use of pure functional ultrasound imaging (fUS) [2, 17], a non-invasive technique based on variations in Power Doppler (PD) signals (Figure 1.2). The Doppler effect occurs in presence of moving particles along the path of the traveling US waves, which cause shifts in the

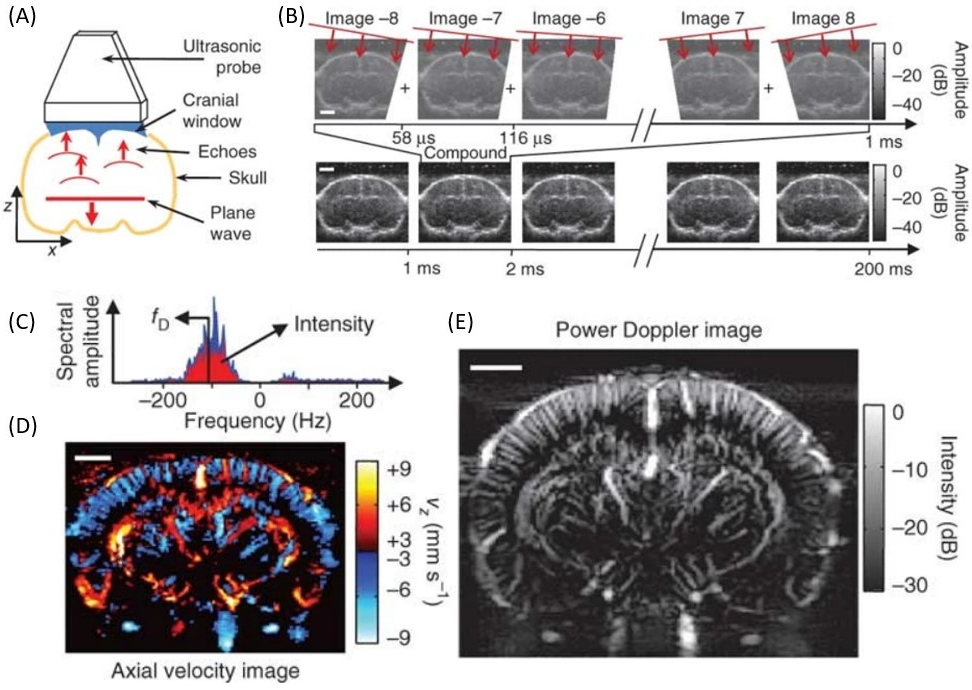

Figure 1.2: fUS neuroimaging based on Power Doppler images. (A) shows a schematic setup to perform fUS neuroimaging; (B) to perform fUS, 17 planar US waves tilted with different angles are emitted into the murine brain. The acquired 17 images of 2 cm × 2 cm are summed up to a compound image acquired in 1 ms. The entire fUS sequence consists of 200 compound images acquired in 200 ms; (C) Frequency spectrum of sB, from which two parameters are computed: the central frequency fD, proportional to the blood velocity axial to the z-axis (D); and the intensity (power Doppler), proportional to the CBV (E). Scale bars, 2 mm [17]

frequency of the detected waves. Such effect is obtained in the cerebral networks where the moving particles are the red blood cells flowing through vessels, causing rapid variations in the detected US which are linked to the fast changes in cerebral blood volume (CBV) and cerebral blood flow (CBF).

Neuroimaging based on fUS showed superior spatiotemporal resolution, allowing real-time visualization of fast hemodynamics usually nondetectable with fMRI. However, it revealed itself to be mainly only sensitive to variation in CBV [17, 18], losing information deriving from O_2 level changes in the blood. In addition, the main limitation of fUS is represented by its inability of rendering 3D structures in real-time: only single coronal slices are provided, of average effective thickness of around 0.3mm [2]. Moreover, this technique cannot be performed on humans without getting invasive with surgeries like craniotomy [19]: the presence of the skull represents a great limitation for the US waves, and a cranial window is needed to reach the deeper structures of the brain with good resolution.

1.2 Optoacoustic Neuroimaging

Lately, multispectral OA tomography (MSOT) has emerged with great potential as a noninvasive preclinical neuroimaging tool, thanks to the combined benefits of specific optical contrast and high resolution of low scattering US in deep tissues, which allow entire brain visualization in small animals.

OA relies on powerful short pulsed laser emission, which allows imaging of specific molecules. According to the employed wavelength, it is possible to reach deeper levels in the tissues (Figure 1.3).

MSOT allows acquisition of 5D data, thus making it possible to visualize structures in three spatial dimensions, in real-time and with multispectral information collected in the near-infrared spectrum. By decomposing the according signals according to the used wavelengths, it is possible to detect single contributions of HbO and HbR, granting final recording and direct measuring of blood oxygen saturation, CBV, and total hemoglobin (HbT) [1, 21, 22] Figure 1.4.

OAI is also comparable to fUS in terms of spatiotemporal resolution, achieving a sub-millimeter level of details (in the range of 100 µm), typical of only microscopy

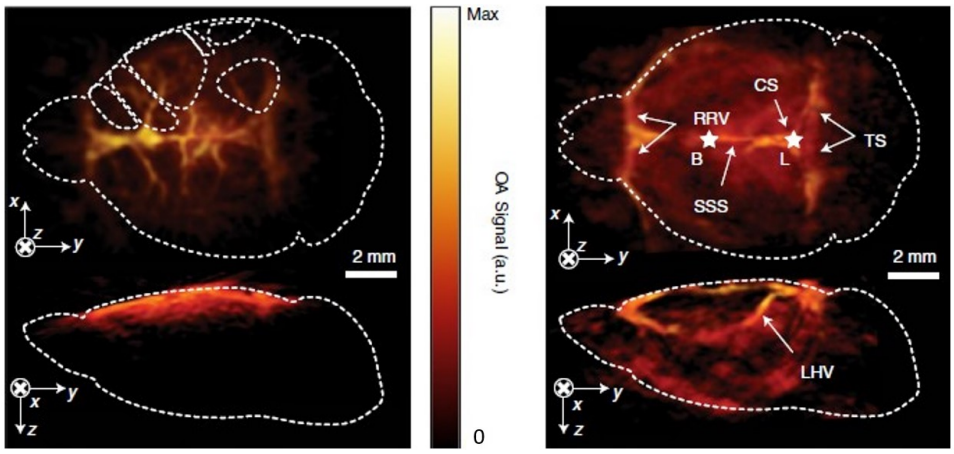

Figure 1.3: OA preclinical in vivo neuroimaging. The images represent maximum intensity projections of non-invasively in vivo recorded OA data from the murine brain at 488nm (on the left) and 650nm (on the right).
According to the chosen wavelength, different imaging depths are achieved, i.e. 1-2mm depth when investigating at 488nm and ∼7mm at 650nm. Some anatomical reference points are indicated: white stars labeled B and L, respectively indicate bregma and lambda skull landmarks; other acronyms stand for CS, confluence of sinuses; LHV, longitudinal hippocampal vein; RRV, rostral rhinal vein; TS, transverse sinus [20].

analysis, in macroscopic brain areas visualization [23, 24, 25] , and imaging capability fast enough to match in vivo neural activity shown by calcium dynamics [24, 20]. In addition, the highly specific optical contrast helps observe signals from cortical venules and smaller arterioles, subjected to bigger changes than the main vessels, which was not achievable with other imaging methods [26, 27]. Preliminary studies also showed OA ability in imaging patients with ferromagnetic implants, which could not undergo fMRI examinations [28].

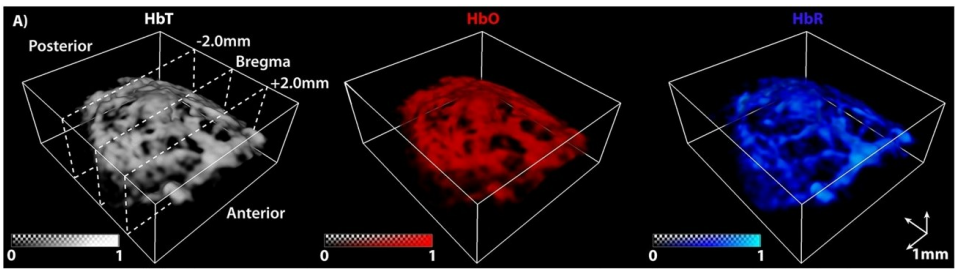

Figure 1.4: MSOAT of murine brain.
Left image represents HbT total contribution. After performing spectral unmixing it is possible to differentiate between single distributions of HbO and HbR (central and right reconstructions). [1]

1.3 Aim of the Thesis

The abilities to visualize real-time volumetric images with high spatial resolution define OAI to be superior to other competing in vivo preclinical neuroimaging techniques [24, 20, 26, 29]. However promising, state of the art of OA neuroimaging reports some limitations.

First of all, the pulsed light source does not propagate uniformly to the desired target, creating a pattern at the interface with the sample. This results in a biased distribution, with hotspots in which higher energy accumulates. Significant light absorption by preferential sites of the brain can have a conditioning effect on the final image, strongly influencing the local light fluence and thus the amplitude of the signals recorded from deeper tissues [30] (Figure 1.5).

Moreover, laser-emitted light fluctuates over time, affecting the energy and spatial distribution of the emitted pulses. This results in the inability to reliably describe small changes in neuronal activity since the variations in real-time illumination might cover ongoing processes or enhance unreal changes.

Thus, the work proposed in this thesis aims to investigate the nature of the light fluctuations affecting OA neuroimaging and tackle them both from a hardware and software perspective pursuing the quest for a more homogeneous and stable illumination profile.

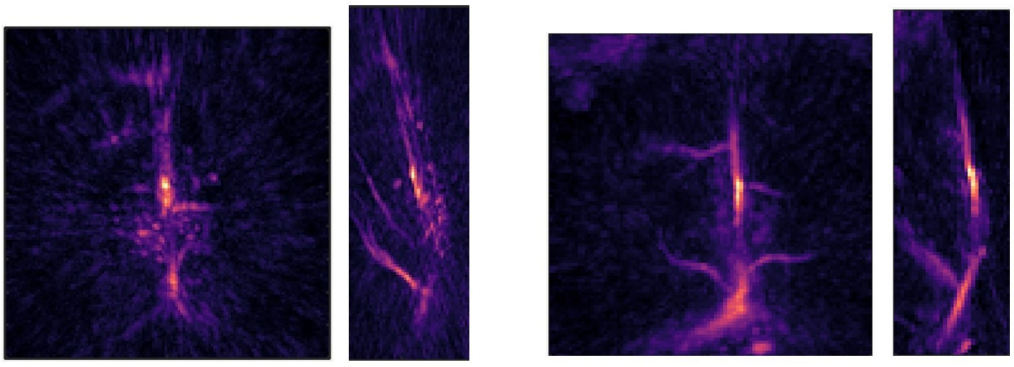

(A) (B)

Figure 1.5: Comparison of OA images of murine brain vasculature.
(A) corrupted acquisition, affected by presence of microbubbles which destroy the final image; (B) good OA acquisition of the mouse brain, where it is possible to evaluate hemodynamics changes.

1.4 Thesis Outline

This thesis is organized as follows: at first, Chapter 1 presented an introduction to the topic of this work, beginning with an overview of the state of the art of neuroimaging methodologies. Eventually, the aim of the thesis is proposed.

Chapter 2 shows an overview of OAI, describing the history and background working principle.

Chapter 3 follows, explaining the methods employed during the research. It presents a description of the instrumentation for OA neuroimaging hardware setup, as well as the performed experiments to investigate the problem and test alternatives. It also explains the ideas behind and the data analysis performed to compare the obtained results.

Chapter 4 describes the idea and gives motivations behind the proposed hardware and software alternatives tested.

Then, Chapter 5 presents and compares the results obtained throughout the different phases of the work.

Chapter 6 contains a discussion on the results achieved, showing the impact and limitations of the work.

Eventually, Chapter 7 concludes the thesis, summarizing the proposed corrections and their effects, suggesting directions for future works.

Chapter 2

Background

Synopsis In this Chapter the theoretical information about OAI is provided as background explanation, describing in detail the imaging process and general hardware setup.

2.1 Fundamentals of Optoacoustic Imaging

Optoacoustic (OA) imaging, also known as photoacoustic imaging, is an emerging imaging technique, which allows non-invasive visualization of biological structures at superficial- and depth levels in the tissues. This hybrid technology benefits of combined advantages, derived from the ultrasound property of low scattering, and high sensitivity and specificity of light absorption within biological tissues.
Hence, with OAI it is possible to visualize structures with high optical contrast for imaging depths up to a few centimeters: the optical diffusion limit of 1 mm in biological tissues can be exceeded, as sound scattering in tissues results in several orders of magnitude lower than optical scattering [31].

The working principle of OAI is based on the optoacoustic effect, first discovered by Alexander Bell in 1880 [32]. While experimenting with a photophone, he noticed how it was possible to originate sounds through the action of a variable light, in mediums of different nature. Further investigations led by various scientists in the next years linked the reason of the sound origin to the thermal changes caused by the light source [31].

Although the OA effect was first discovered more than 100 years ago, OA imaging

as it is known today was not possible until the late 1980s, with the advent of lasers as a light source. Using "high-intensity ultrasonic radiation or therapeutic levels of ionizing radiation", the aim was to deposit energy in the tissue in order to generate a sound wave and evaluate materials in a non-destructive way [33].

After understanding the theory behind OA effect generation, and more in particular the physical relation between the morphology of the obtained sound waves, the geometry of the target object, and the duration of the exciting laser pulse, it has been possible to formulate the first reconstruction algorithms, aimed to allow visualization of original size and shape of the emitting body or tissue, by measuring the sound waves it creates.

The theoretical concept behind the generation of OA signals is based on the OA effect (Figure 2.1). The process can be represented as a chain of subsequent events, where each step is the trigger input of the following one.

The imaging process starts with the use of a *laser source* to illuminate the target sample. The laser is operated in pulsed modality, with pulses of nanoseconds duration, in order to avoid considerable thermal diffusion and at the same time allow light penetration in the tissue.

Photons interact differently with the cells they encounter along their path: some biomolecules, such as hemoglobin, melanin, water respond to specific wavelengths and absorb them. Such *light absorption* causes *thermoelastic expansion* of the molecules, followed by a pressure increase that originates *ultrasonic pressure waves*.
The US pressure wave travels from its point of origin to the outside, where it is detected by apposite *US transducers* and converted into a digital signal.

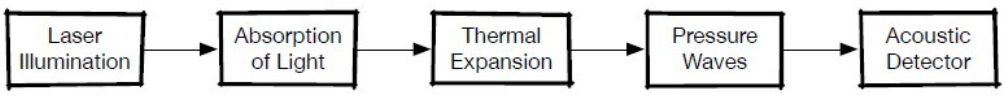

Figure 2.1: Schematic representation of the fundamental steps necessary to perform OAI. The technique relies on powerful short laser-emitted light pulses, which are directed onto the target tissue. Here the light is absorbed by specific chromophores, which are then subjected to thermal expansion. in response to a pressure increase, pressure waves are generated and detected by external acoustic detectors.

The ultrasonic waves carry important data about the original morphology, composition, and location of the inspected tissue, which can be interpreted employing mathematical algorithms. In OA tomography, the detectors are multiple and located around the sample in specific geometries to allow optimal information transmission. In this way, through image reconstruction, it is finally possible to map the original spatial distribution of photons absorption in target tissues.

Moreover, investigating the samples through multiple optical wavelengths in a single acquisition further allows functional and molecular imaging by identifying the specific absorption of the various molecules composing the tissue. This particular imaging modality is known as multispectral optoacoustic tomography (MSOT).

Clearly, in order to be performed, OAI relies on the use of specific instrumentation, which will be illustrated in detail in the following chapters. It is interesting to notice, however, how it is possible to recognize subpaths of different natures in the chain of events described above. In fact, the optoacoustic path can be conceptually divided into 3 subsections: the optical path, the acoustic path, and the electronic path.

1. Optical Path: it represents the first processes that allow OAI, where light is generated from a laser-based source and travels through a designed path to reach the tissues. Although it would conceptually be possible to directly aim the beam to the target sample without intermediate elements, this would result in energy loss and limited ability to control the beam. For this reason, usually optical fibers bundles are used, to direct the light to the desired spot. Further details on the hardware for the optical path will be given in the following chapter.

   Once light reaches the target, it is significantly affected by the different tissues composition and density, which results in a quick and high attenuation. This latter can be modeled as an exponential decay and can be described using the Beer-Lambert law, where fluence decreases along with the traveled distance, according to the crossed medium properties [33]. Physical causes of attenuation are to be attributed to two main factors, namely scattering and absorption, with the first one playing a major role in signal loss [34].

   In physics, scattering refers to the change in the direction of propagation of

moving particles, following particles' interaction or physical collision. Here, photons are subjected to deflection in direction due to the composition and density of the tissues they're propagating through, in a measure proportional to the total traveled distance. The structural proteins present in the living tissues constitute major scattering centers, affecting light penetration and spatial resolution. Biological tissues like the brain or skin are known to be highly scattering, thus leading to a high risk to obtain blurred images.

Absorption, on the other hand, happens when photons interact with specific chromophores present along their pathways. Biological tissues present a variety of such light-absorbing molecules, which respond to specific wavelengths by absorbing the incoming photons (Figure 2.2).

For example, living tissues are made for the majority of water: this results in transparent to visible light but absorbing in the infrared spectra. Hemoglobin instead, absorbs light at visible wavelengths, and so do other pigment cells such as melanocytes.

However, the choice of the explorative wavelengths must also be made taking into account the reachable depth: the shorter the wavelength, the more difficult it becomes to reach in-depth structures, as light diffusion becomes prevalent on penetration.

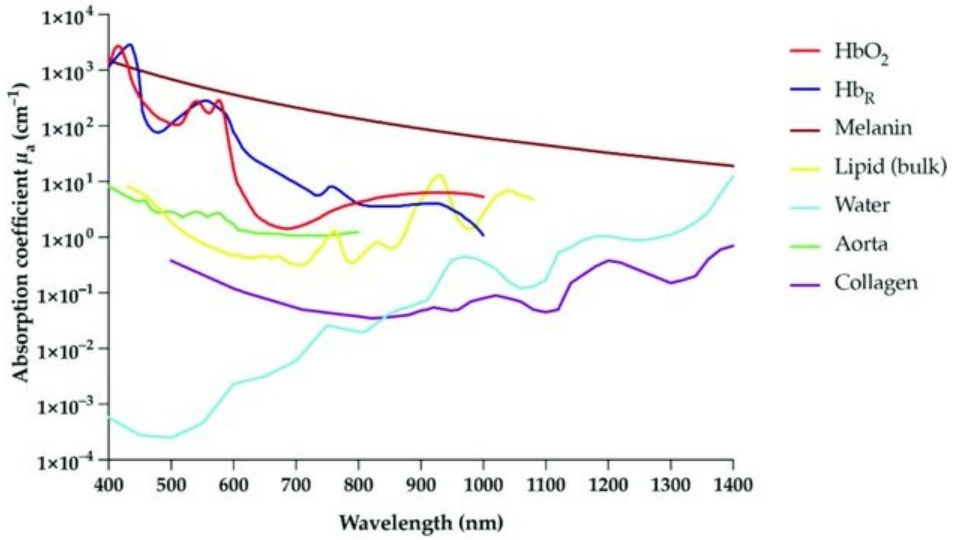

Figure 2.2: Biomolecules absorption coefficient in relation to different explorative wavelengths. [35]

2. Acoustic Path: when the chromophore is hit by photons of compatible wavelength, it absorbs it causing a small variation in pressure exerted on the surrounding structures. This pressure shift generates detectable acoustic waves, beginning the acoustic pathway. The conversion of energy to pressure can be quantified and it is identified in the Grüneisen parameter [31, 33].

   The signal transduction thanks to the OA effect is what de facto allows the strengths of OA imaging: the optical path allows obtaining contrast in the image, thanks to the different chromophores responses to specific wavelengths, while the acoustic path makes OAT inherently non-sensitive to light scattering in the tissues, to the advantage of penetration depths [31].

   Once generated from the photons absorption, the acoustic wave, or US wave, propagates in the sample, and externally, carrying information related to location, size, and reflectional properties of the molecules which caused its origin. The amplitude of the traveling wave depends on several factors, such as both acoustic and optical properties of the samples, and the generated light fluence. Withal, such wave can propagate almost scatter-free, as it is known that, especially in biological structures, US scattering is almost 3 order of magnitude lower than optical scattering [36], reason for which it is possible to visualize also deeper tissues.

   However, US waves are not immune to absorption. Signal loss can be once again described using an exponential decay, where signal reduction increases the frequency, the traveled distance, and the properties of the crossed tissue. Thus, a compromise must be made between the imaging depth, desired spatial resolution, and acceptable SNR.

3. Electronic Path: thanks to the presence of US transducers, the biological signal, traveling in the form of a US wave, is transduced in voltage signal through the presence of piezoelectric devices. As for any other electronic signal carrying biological information, it must be amplified, converted to digital, and processed in order to finally reproduce the diagnostic image. Amplification is needed to increase the strength of the detected signals, and avoid information loss; however, by increasing the signal amplitude, also the noise is amplified. The choice of the amplifier itself influences the noise transmission: choosing

appropriate low noise amplifier (LNAs), it is possible to reach an optimal trade-off between amplification of the signal and low SNR deterioration [33]. First filtering procedures might also be carried out before conversion, to reduce the unnecessary noisy components and keep the tissue-describing ones. After amplification, the signal can be transmitted to the analog-to-digital converter (ADC) device built inside data acquisition systems (DAQs), to be digitized. ADC devices are chosen taking into account inherent properties:

- Resolution: defining number of available bits, typically 10 to 14 bits in modern OAI systems [37];
- Sampling rate: set in accordance to various aspects, such as the imaging modality, the specific transducer used, and the Nyquist–Shannon sampling theorem [38], for which the sampling frequency should be at least twice the maximum frequency in the signal's frequency band. Typical values in modern OAT are less than 40 Msps [33];
- Transmission bandwidth: crucial element in defining the speed of signal transmission in OAT. Given the high number of used detectors (usually 512) and the frame rate up to 100 Hz, OAI generates a very large amount of received data, which must be taken into consideration when choosing the electronic components [33, 39].

After ADC conversion, the new digital signals are transferred to a PC to be processed and then reconstruct the original images. Thus, signals are filtered to further reduce the noise components and given as input to mathematical algorithms. The most commonly implemented is the back-projection method [40], where each OA signal is projected into a volumetric image, with all signals contributions adding up to the final 3D rendering. The quality of the reconstruction is slightly expendable in favor of speed reconstruction, thus allowing real-time visualization of structures at a high frame rate when using a GPU [41].

Chapter 3

Methods

Synopsis This Chapter introduces and discusses the approach followed to quantify and correct the laser fluctuations that affect OAI.

Its first section, Section 3.1, begins with an overview of the instrumentation for OA neuroimaging, useful to understand the hardware setup implemented in the experiments.

Afterward, Section 3.2 proceeds to illustrate the steps followed to characterize the beam profile at the input and output of the light transmission path.

Then, Section 3.3 and Section 3.4 describe respectively the *phantoms* and *in vivo* experiments performed.

Eventually Section 3.5 describes the statistical analysis performed on a spatial and temporal point of view on the beam fluctuations.

3.1 Instrumentation for Optoacoustic Neuroimaging

As previously illustrated in Chapter 1, the OA path can be conceptually divided into 3 subsections: the optical path, the acoustic path, and the electronic path, each characterized by relative hardware specific to manage signals of different nature. This thesis focuses mainly on the first chain of events, namely the optical path.

To trigger the OA effect, an initial light source is needed. In particular, modern OAI systems are based on the use of a monochromatic, coherent, and directional source, namely the laser. Thanks to these features, laser-emitted light results in a beam of single-wavelength waves traveling in phase with each other, and it is characterized by low divergence, which allows maintaining high beam intensities over long ranges.

The operating modality of the laser must be set to pulsed, in order to obtain the required nanosecond light pulses in the millijoule range able to generate OA effect without harming the tissue [29]. In particular, the lasers available in the lab for experimental purposes are optical parametric oscillator-based (OPO) Spitlight lasers, (Innolas Laser GmbH, Krailling, Germany), fast enough to reach 100 Hz repetition rate and tunable in two ranges respectively:

- visible range: 380 - 680nm.
- near-infrared range: 650 - 1100nm.

After choosing the wavelength and generating the initial beam, laser-emitted light must be directed to the target samples to allow tissues investigation.
For this purpose, multimodal (MM) optical fiber bundles are used (Figure 3.1); in this way, it is possible to avoid energy dispersion, and the light beam is correctly delivered to the object of interest through a controlled path. They additionally offer great flexibility, allowing adaptable arrangements and increased safety for experimental purposes [33, 42].

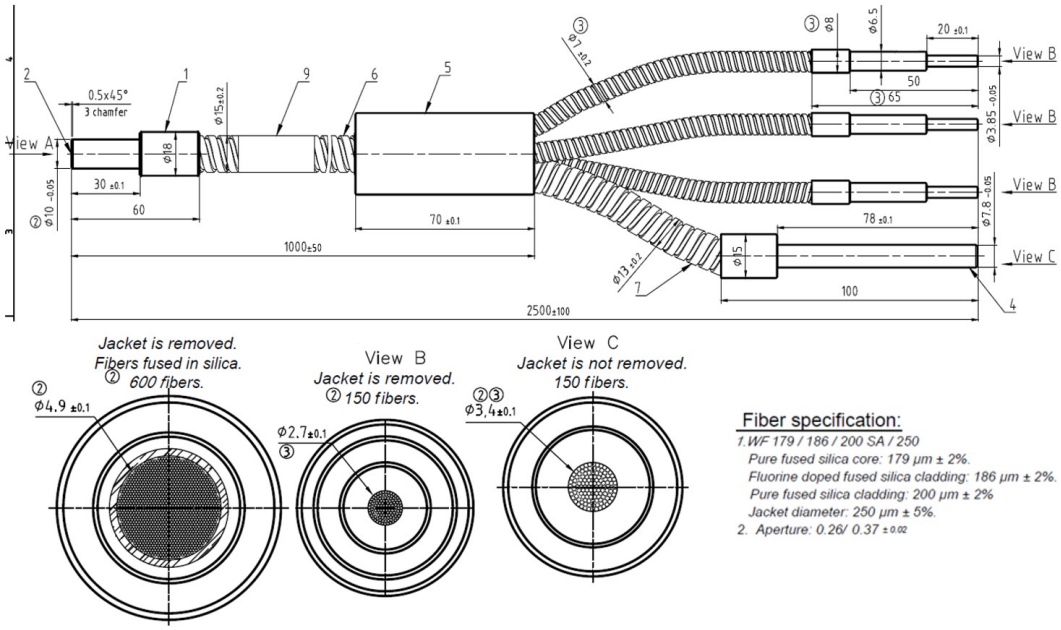

Figure 3.1: Technical draw and specifications of the MM fiber bundle used during the experiments. The top draw reports the entire bundle sketch, while in the bottom part are reported the input and different tails frontal views.

In particular, the fiber bundle used in the experiments is a custom-made bundle of 600 fibers of a pure fused silica core of 179μm (CeramOptec® GmbH, Germany). The entire fiber bundle design consists of one main output tail with a diameter size of 7.8mm, and three minor ones of 3.85mm in diameter each. The fibers are equally subdivided along the path so that eventually the 4 tails contain 150 fibers each.

MM fibers are recommended for OAI setups as they result superior in power transmission, and can couple efficiently light even when not in the optimal configuration. For these reasons, they are preferred to other types of existing fiber, e.g. the conventional single-mode (SM) fibers, whose core appears to be too small to handle laser power for imaging purposes, affecting the final spot size with artifacts such as diffraction or lens aberration [42].

Beneficial to maintaining a fixed arrangement and also allowing as much as possible repeatably of experiments, the MM fiber bundle outputs are inserted in an appropriately designed cup, which is also the house of the US detectors (Figure 3.2 and Figure 3.3). In this way, the illumination angle of the output tails is fixed, designed

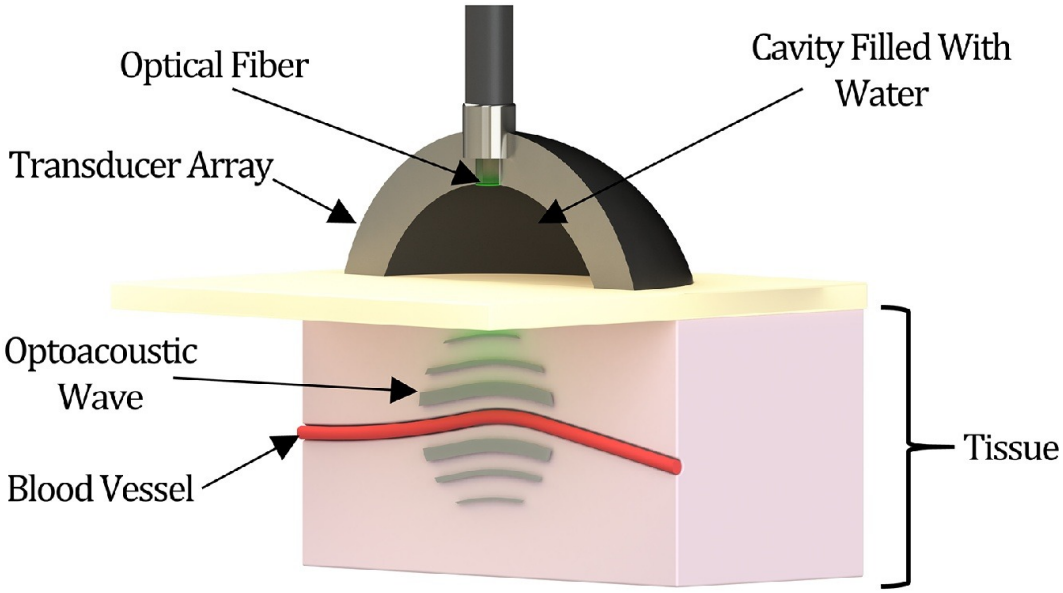

Figure 3.2: Representative drawing of OA neuroimaging setup based on a three-dimensional hemispherical transducer array. The volume between the array and the tissue is filled with water and sealed with a plastic film to provide acoustic coupling. Laser light is delivered through the MM fiber bundle tails. Here only the main output which provides central illumination is shown. The three smaller tails face equidistant from the lateral surface. [43]

to be in the optimal configuration, in terms of balanced illumination of all the areas in the target imaging sample [33].

At this point, granting light exposure on the target sample, the conditions to allow OAI are satisfied. As illustrated in Chapter 2, thanks to the OA effect the biological information travels back to the OA system in the form of US waves.

One general issue when dealing with US is the reflective behavior to which acoustic-nature waves are affected when traveling through mediums with different acoustic impedance. This resistance-like action opposed by the medium to the passage of the acoustic wave is defined as the product between the medium density r and the propagation velocity c. Translating this effect into a practical scenario, it is easy to understand how having the target object immersed in a medium with very low acoustic impedance which is air, would hamper US transmission to the DAQ.

Therefore, to allow correct propagation and detection of the returning US waves, the cup is filled with water and sealed at the bottom with a transparent film. This

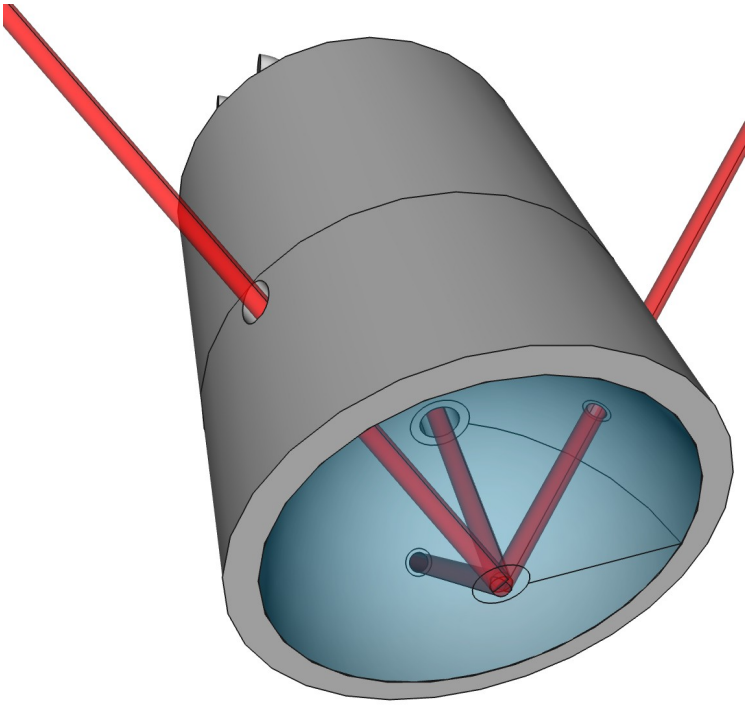

Figure 3.3: CAD design of custom made USD cup (three-dimensional hemispherical transducer array). It is possible to notice the disposition of the output tails of the MM fiber bundle, represented by the red axis. The inside of the cup is filled with water to allow US propagation.

soft boundary represents the interface at which the target sample is posed.

When investigating biological samples, such as the murine brain, a further element essential to grant a correct transmission of the signals is the US gel. This is needed to reach the optimal coupling efficiency between the US propagation in water and the tissues. In fact, the reflection coefficient for acoustic waves at the soft tissue-air interface is around 99.9%. This means, almost the entirety of the wave gets reflected back into the tissue, and essentially no signal manages to propagate in air.

Given the *in vivo* applications of OAI, it would not be possible to just submerse the target in water. By applying the coupling gel, it is possible to eliminate air in the region surrounding the tissue; moreover, reducing the differences in the acoustic impedance of the mediums, it is possible to achieve better transmission of the US waves through the water membrane to the transducers.

3.2 Illumination profile characterization

Given the fundamental role of the input light source, it is important to try to determine the beam characteristics, as its initial profile is the first factor playing a role in the final illumination to which the target is exposed.

It is not trivial to determine one single objective parameter with which to evaluate the beam quality [44]: one of the most commonly used is the M^2 parameter, proportional to the product of beam width and angle of divergence. It allows to get a measure of the beam propagation and foretell how fast it will diverge. The lowest the value of M^2, the less diverging the behavior of the beam; $M^2 = 1$ defines the propagation of an ideal gaussian beam, representing the possible best profile for any laser beam [44].

However, M^2 value alone is not able to fully describe a beam, let alone allow reliable comparisons. Thus, to evaluate it, it would be necessary to analyze the near-field intensity profile along with the far-field behavior [44].

On the other hand, relying on the knowledge of the initial beam characteristics only is not enough. That is because, as previously described in Section 2.1, light is not directly focused on the target, rather it is directed to it through a specific pathway that is the MM fiber bundle. Even if not taken for granted, it is easy to imagine that the shape of the light beam entering the fiber might not be transmitted in the same way to the outputs.

The beam intensity profile at the input side, determines the upstream modes distribution [45]. The spatial beam quality, the M^2 factor above, measured at the end of the optical fiber depends on the distribution of the modes propagating within the fiber itself. Also, it appears to be linearly proportional to core size and partially affected by the total size of the fiber, which affects in turn fiber stress and micro bending [42]. Another factor to take into account is the coupling coefficient, defined as the ratio between the input beam waist and the core radius [46].

For this reason, in order to characterize the beam shape, the behavior of its profile over time has been studied at the beginning of the path, along the way, and at the target interface. Afterward, statistical analysis has been performed on the acquired data at the source and target level of illumination, as will be described in the next sections.

3.2.1 Input beam

The first step taken in the investigation of laser fluctuations was to study the beam profile directly at the source.

In the lab, two lasers are available, one operating in the visible range (VIS), and the other in the near-infrared (NIR) range. Three representative wavelengths have been chosen, the first 2 belonging to the visible spectrum, thus investigated using the VIS laser, and the latter belonging to the NIR range, investigated on the relative laser:

- DATASET 1: wavelength 1 = 530nm (green)
- DATASET 2: wavelength 2 = 600nm (red)
- DATASET 3: wavelength 3 = 680nm (NIR)

In order to characterize the beam profile at the source of the illumination, i.e. the laser output, a Thorlabs DCC camera (Thorlabs, DCC 3240M) has been used to acquire 2D images of beam fluctuations over time.

The first setup (Figure 3.4) was realized at the output of the visible laser, exactly the same for datasets 1 and 2 while a similar version was recreated at the output of the NIR laser for dataset 3.

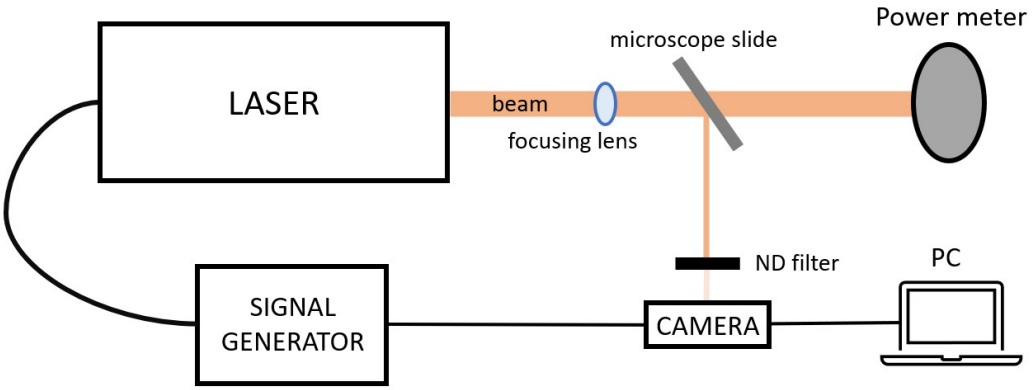

Figure 3.4: Schematic representation of the experimental setup for input beam characterization. Once originated from the laser, the optical beam is focused and then split employing a microscope slide. A low-intensity fraction of the beam is attenuated by passing through an ND filter and directed to the camera to be visualized. The remaining part is instead directed to the power meter, to record the intensity values. The camera acquisition is controlled by a PC, and synchronization with the laser pulsed modality is achieved thanks to the presence of a signal generator.

During the acquisitions, the laser has been operated in pulsed modality at 25 Hz, to allow synchronization with the camera shutter.

To protect the camera and accurately monitor the beam, the following materials were used:

- Focusing lens, needed to collimate the beam and focus it at the center of the path, posed at a distance of 7cm from the laser output;
- Microscope slide of 1mm thickness, which was needed to split the beam and direct around 2% of its original intensity to the camera, preventing damage;
- Neutral density filters (NDFs), to further reduce intensity. Different combinations were used, in particular a combination of ND1 and a camera-custom-made one for wl1 and wl2, and ND2 alone for wl3.

The remaining intensity (∼98%) directed away from the camera, was measured via a power meter to keep track of the original emitted power.

To synchronize the camera acquisition with the laser emitting in pulsed modality, additional control via external trigger was needed. Hence, a signal generator has been connected to the laser trigger and a delay of 30ms was set, in order to create a pulsed modality input for the camera. In this way, the camera was successfully synchronized with the following laser pulse.

The acquisition of the images in *.tiff* format was controlled by a pc, controlling the camera through the Thorlab interface "ThorCam".

3.2.2 Illumination at target

After characterizing the beam profile at the source, the second step concerned the evaluation of light distribution at the end of the optical path, right before the interface with the target. The experimental setup was composed of the following materials, listed in order from the laser output to the target position. A diagram of the setup is also shown in Figure 3.5.

- Focusing lens, needed to collimate the beam and focus it at the center of the path and set at a distance of 7cm from the laser output;

- Microscope slide of 1mm thickness, which was needed to split the beam and direct around 2% of its original intensity to the camera, preventing damage;
- Fiber bundle coupling, to couple the emitted light into the fiber bundle;
- MM fiber bundle custom made for the used cup;
- US detectors cup, filled with DI water;
- Water membrane, a transparent film sealing the bottom of the cup to avoid water loss;
- Neutral density filters (NDFs), to further reduce the intensity, posed right at the top of the camera lens. Different combinations were used, in particular a combination of ND2 and ND3 one for wl1 and wl2, and ND2 alone for wl3.

The camera synchronization and control were done using respectively the signal generator and the ThorCam interface, as in the previous experiment described in subsection 2.2.1.

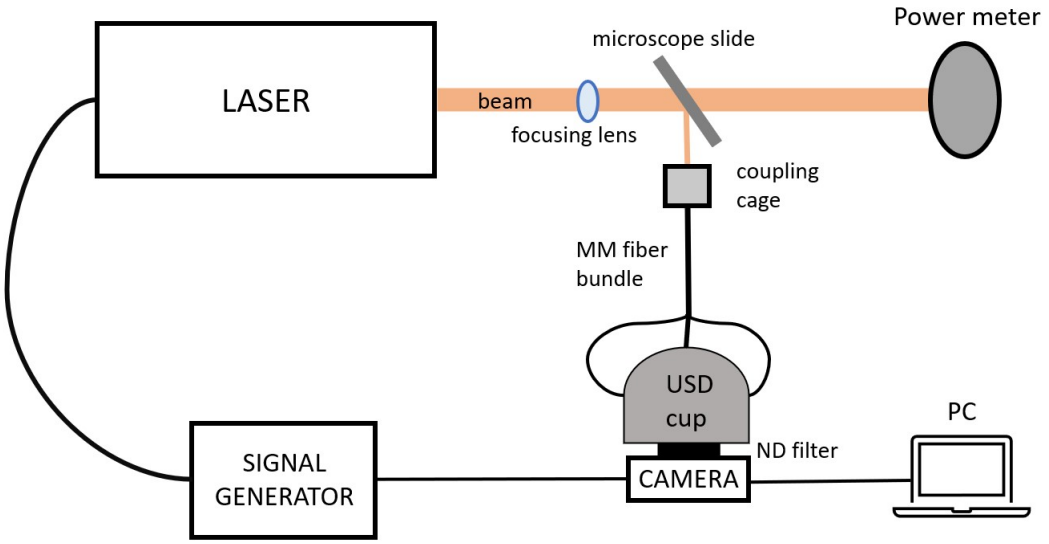

Figure 3.5: Schematic representation of the experimental setup for beam characterization at the target interface. Once originated from the laser, the optical beam is focused and then split through a microscope slide. The low-intensity part is coupled with the input of the MM fiber bundle, which directs light into the USD cup, filled with DI water and sealed with a transparent film. At the bottom of the cup is placed the camera, protected by ND filters. The major part of the beam is instead directed to the power meter, to record the intensity values. The camera acquisition is controlled by a PC, and synchronization with the laser pulsed modality is achieved thanks to the presence of a signal generator.

3.3 Optoacoustic phantoms experiments

This experiment aimed to analyzed the OA response in homogeneous samples made with different concentrations of agar and ink.

The phantoms used were custom-made in the lab. For the preparation procedure, a base of 300 ml of DI water was used to dissolve 4.5g of agar, creating a 1.5% agar concentrated solution. A total of 4 phantoms were created, testing two different ink concentrations and the effects of two different top layers.

To create the phantoms (Figure 3.6), petridishes of a total volume of 23ml were used. The ink concentrations employed were:

- concentration 1: 0.1% ink and remaining volume of clear agar;
- concentration 2: 0.05% ink and remaining volume of clear agar.

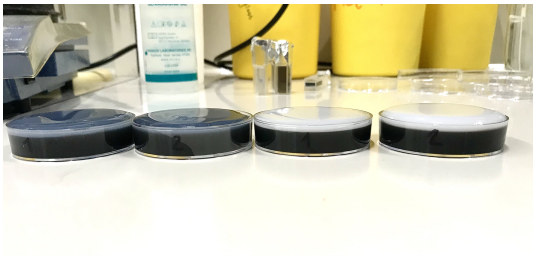

(A)

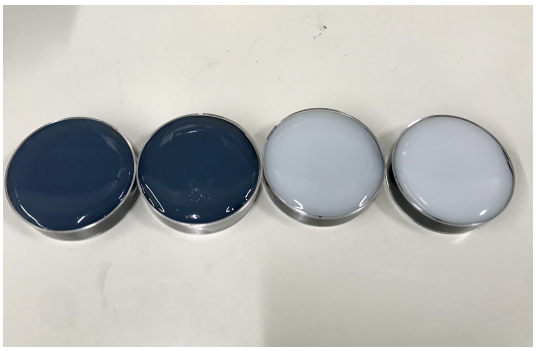

(B)

Figure 3.6: Frontal (a) and top (b) view of the experimental agar phantoms.
From left to right, are shown first the phantoms with clear agar top layer, first one being the one with ink concentration 1, second one the one with ink concentration 2, then as third the phantom with ink concentration 1 and superficial layer made with intralipid, and finally as fourth the phantom with ink concentration 2 and superficial layer made with intralipid.

The superficial layer, on the other hand, was created in two ways:

- agar: only 3% concentrated clear agar solution;
- intralipid: clear agar was mixed with a quantity of intralipid correspondent to 1.5% of the total solution, to create a scattering layer aiming to mimic biological tissue.

According to the phantom, one of the two different solutions was used to fill the superficial part of the phantom, creating a dome-shaped surface.

In order to perform OAI of the phantoms, the experimental setup (Figure 3.7) was realized employing several materials.

In particular:

- Focusing lens, needed to collimate the beam and focus it at the center of the

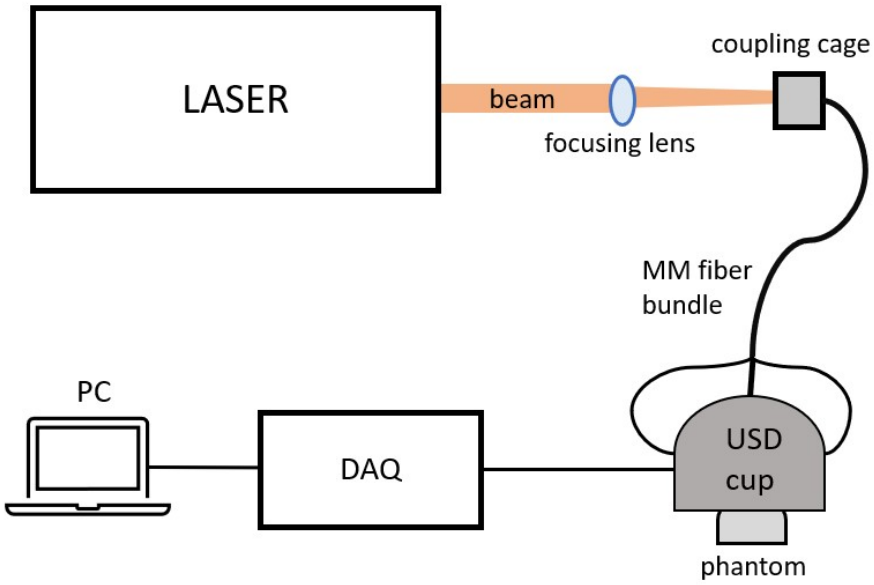

Figure 3.7: Schematic representation of the experimental setup for OAI.
The setup is the same used during the beam characterization phase, but in order to trigger OA effects in the phantoms higher energy is needed. Thus, the microscope slide is removed, and the free beam is focused employing the lens and directly coupled with the input of the MM fiber bundle, which directs light into the USD cup, filled with DI water, and sealed with a transparent film. At the bottom of the cup is placed the phantom. US waves originated through OA effect are detected by the US detectors within the cup, and the registered raw signals are sent to the DAQ, and eventually to the PC to be reconstructed.

path and set at a distance of 7cm from the laser output;;

- Fiber bundle coupling cage, to fix the coupling of the emitted light into the fiber bundle;
- MM fiber bundle;
- US detectors cup;
- Spherical array holder;
- DAQ;

Furthermore, to investigate the response to different wavelengths, MSOT was performed by operating the laser at different wavelengths. The chosen ones were 730nm, 755nm, 780nm, 800nm, 850nm which are the most commonly used to investigate biological tissues hindered at deeper levels. The laser (fast NIR OPO Spitlight laser) has been operated in pulsed modality at 100 Hz.

3.4 Optoacoustic in vivo experiments

OAI of in vivo mouse brain was performed in order to compare the acquisition at different coupling distances. The same setup and list of materials as for the phantoms acquisition was kept (Figure 3.7), with few exceptions.

The concave lens was substituted by different coupling distances. To test the coupling efficiency, two distances were set between the focusing lens and the coupling cage (input of the MM fiber bundle).

After checking the laser alignment, the coupling positions were chosen by checking the shape of the beam at the fiber bundle input (d1) and checking the energy at 10Hz by means of the powermeter (d2). The PRF was then shifted to 100Hz to record the energy transmitted at 700nm.

The selected position were at distances:

- d1 = 23mm, energy at 100 Hz = 10.4mJ;
- d2 = 42mm, energy at 100 Hz = 14.8mJ.

From the laser casing to the focusing lens a distance of 30mm was maintained.

Additional steps during the experiments were performed for animal imaging preparation. The mouse was anesthetized with a 3% initial induction of isoflurane, gradually lowered to 1.5% at the start of the experiment.

In vivo preclinical experiments require the presence of additional instrumentation to take care of the mouse and monitor its well-being (Figure 3.8). Physiological parameters of the mouse such as heartbeat and body temperature, were monitored with PhysioSuite (Kent Scientific, Torrington, USA).

The mouse was placed on a heating pad to keep body temperature stable, and a 3D manual stage was used to place it at the right interface location under the USD cup. Stability was assured through the use of a black stereotactic head holder custom-made for OAI.

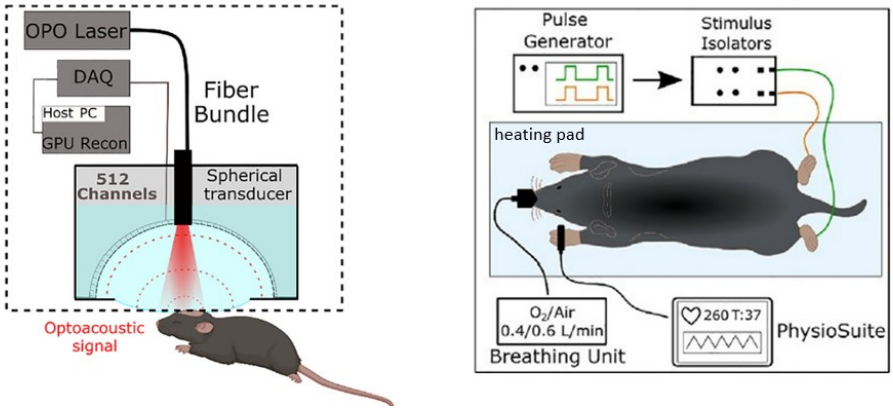

Figure 3.8: Experimental setup for in vivo preclinical OA neuroimaging.
On the right side it is shown the position of the mouse during OA neuroimaging. During this experiment, scalp removal was not performed.
On the left, the instrumentation for animal care, composed of a heating pad, breathing unit, and PhysioSuit for vital parameters monitoring. External stimuli were not applied during this experiment [2].

3.5 Data analysis

After acquiring the images through the camera and the OA system, the data, respectively in *.tiff* format and raw OA data, have been exported on a PC to be analyzed. In particular, the types of acquired data are:

1. camera images: the *.tiff* data contain information of 2D images acquired for a certain temporal window.
2. OA data: after reconstructing the data through the universal back-projection algorithm, the OA information is stored in 4D data, where the first 3 are the spatial dimensions, and the latter the time evolution. When MSOT is used, an additional dimension is added to the data, relative to the specific wavelength used.

The data analysis has been conducted on Matlab, focusing on the extraction of statistical parameters to quantify the beam variations in time and space.

The main parameter taken into account is the standard deviation (std): it is defined as the dispersion of a set of data from its mean. It can be calculated as follows,

$$std = \sqrt{\frac{1}{N-1}\sum_{i=1}^{N}|x_i - \mu|^2} \tag{1}$$

where N is the number of observation of a dataset, x is the vector of observed values, and μ is defined as the *mean* of x:

$$\mu = \frac{1}{N}\sum_{i=1}^{N} x_i \tag{2}$$

In general, the standard deviation represents a very useful parameter in estimating the behavior of a dataset, as it gives an evaluation of how "spread out" a dataset

is. The largest this value is, the more dispersed the data appears to be, in relation to the mean of the dataset. In this case, by quantifying the standard deviation in a set of recordings, it is possible to evaluate the spatial and temporal fluctuations that affect OA systems.

3.5.1 Spatial fluctuations analysis

In order to evaluate the spatial fluctuations, the statistical parameters have been extracted considering the evolution of every single pixel or voxel over time. In other words, the temporal evolution of each basic element has been considered as a dataset, and the standard deviation has been then computed on such a dataset. In this way, it is possible to understand the behavior of each pixel or voxel along time, and compare it with all the others forming the final image or volume, so that to evaluate precisely the spatial differences of the inspected sample.

In addition, through the use of histogram plots, it is possible to visualize the distribution of the spatial std and evaluate whether the evolution of the image is homogeneous. In fact, it is possible to consider a sequence of images not affected by spatial variations, as a sequence of images obtained by scaling one reference static image for a vector of varying amplitude. Thus, it would be possible to define the vector of observations for one pixel, as

$$x_i = x \cdot A_i \tag{3}$$

where x represents the reference static pixel, and A the vector of temporal variations. Subsequently, it would be possible to write the *mean* of the vector x_i as

$$\mu = x \cdot \frac{1}{N} \sum_{i=1}^{N} A_i \tag{4}$$

given that x represents actually a constant.
Considering the definition of standard deviation defined in Eq. 1, and substituting Eq.3 and Eq.4 in Eq.1, the same equation can be rewritten as

$$std = \sqrt{\frac{1}{N-1}\sum_{i=1}^{N}|(A_i \cdot x) - (x \cdot \frac{1}{N}\sum_{i=1}^{N}A_i)|^2} \tag{5}$$

Being x the reference pixel, independent of temporal evolution, it can be taken out of the sum, resulting in

$$std = x \cdot \sqrt{\frac{1}{N-1}\sum_{i=1}^{N}|A_i - \frac{1}{N}\sum_{i=1}^{N}A_i|^2} \tag{6}$$

At this point, the standard deviation of the pixel along time appears to be given by the product of a constant (the reference value of the pixel) and what is actually the standard deviation of the temporal variation vector.

For this reason, it is possible to normalize the std of a pixel by dividing its std by a reference value, and finally obtain the distribution of the standard deviation, normalized and non affected by the initial intensity profile. Through the use of histogram plots, it is possible to have a visual impact of the presence of fluctuations: the narrower the distribution, the fewer spatial variations would be present, as it shows how all the pixels behave in the same way.

3.5.2 Temporal fluctuations analysis

To determine the temporal variations, the statistical parameters have been computed along the temporal axis: for each instant of time, the computed values represent the behavior of the entire illuminated area in that specific temporal frame.

Thus, the temporal std describes the inhomogeneity of the images or volumes for

each acquisition instant.

Besides this, also temporal correlation has been evaluated. The idea behind this analysis was based on checking whether it was possible to define the temporal correlation between two different regions in the target. In other words, to understand how the illumination in two different pixels in one image changed over time, and whether it changed in the same way even in pixels/voxels distributed in different regions. A good correlation between two pixels or two regions would mean that the temporal variations in intensity from frame to frame would be similar, or proportional, in the whole image.

For this reason, different regions in the image have been selected as reference ROIs. When dealing with 2D images acquired with the camera, the chosen size for the ROI was 20x20 pixels. Being each pixel of 5.3µm, the chosen ROI were squares with sides of around 106µm, comparable with the spatial resolution of modern OAI systems. When dealing with OA reconstructed data, instead, each voxel was considered on its own, to not affect spatial resolution.

The regions were selected in different areas of the image: one in the centre, miming the target object, and 3 in the peripheral area with different illumination intensities.

The analysis has been conducted using the Pearson correlation coefficient, able to measure the linear correlation between two sets of data.
In statistics, the Pearson correlation coefficient between two random variables with N scalar observations, is defined as

$$\rho(A,B) = \frac{1}{N-1}\sum_{i=1}^{N}(\frac{A_i - \mu_A}{\sigma_A})(\frac{B_i - \mu_B}{\sigma_B}) \tag{7}$$

where μ_A and σ_A are defined as the mean and standard deviation of A respectively, and similarly μ_B and $\sigma_B$represent the mean and standard deviation of B.
The values of the coefficient ρ can range from -1 to 1. A negative unitary correlation (-1) represents a direct, while 1 indicates a direct, positive correlation negative correlation. In case $\rho = 0$ no correlation is found between the datasets.

Chapter 4

Fluctuations correction

Synopsis This chapter presents the corrections performed on the system.

In particular, Section 4.1 describes the hardware corrections, while Section 4.2 deals with the software correction.

4.1 Hardware corrections

In order to reduce the presence of noisy elements, and aim to achieve a homogeneous illumination of the target, some modifications and additional requirements have been added to the setup.

- Water Filtering. To prevent introducing air or other contamination of the delicate components of OA setup for neuroimaging, different treated water qualities have been tested and additional cleaning of the instrumentation has been performed. Specifically, water purity has been taken care of through the use of a degassing machine. In order to further evaluate the performance according to the chemical composition, two different water qualities have been degassed, to reduce the presence of dissolved oxygen, carbon dioxide, and other gasses from water. Choosing water with a reduced percentage of ions provides safety for the transducers, which could be damaged by the deposits of salt present in tap water. Impurities can also become cavitation nuclei in presence of a pressure field, affecting the imaging and ultrasound delivery performance. In particular, degassed DI water and degassed milliQ water have been tested. The machine (Degasi High-Flow 1000) has been let on for 24h to reduce oxygen percentage by about 5 times in the water inside the container.

Additional filtering setup (Langendorff filter of size 5µm) has been implemented on the system, to avoid water contamination by microbubbles. In fact, despite the very small size, microbubbles are powerful US scatterers. When present, they will alter the free propagation of US and deteriorate the image quality. Additional cleaning of the MM fiber bundle output tails was performed using Isopropyl Alcohol, and an ultrasonic cleaner machine, to assure clean conditions of the optical elements. In this way, it is possible to prevent the generation of spurious OA signals at the face of the fiber bundle output.

- Optical Correction. In order to expand monodimensionally the NIR beam, and obtain a more symmetrical beam profile, an additional optical element has been included in the setup. In particular, the lens used was a N-BK7 plano-concave cylindrical lens provided with antireflection coating for 650-1050nm, with focal distance f=-6.35 mm (Thorlabs, Inc., LK1087L2-B). In this way, thanks to the lens properties, it was possible to expand the narrower side of the beam until it matched in size the larger one, achieving a quite round shape.

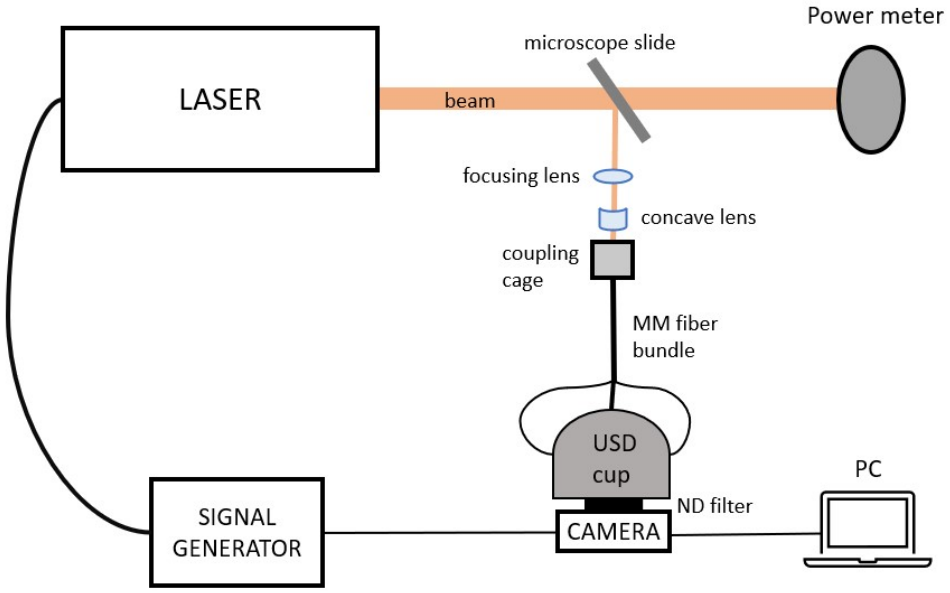

Figure 4.1: Schematic representation of the experimental setup for beam characterization at the target interface when implementing optical correction. The plano-concave cylindrical lens is mounted between the free beam and the coupling cage holding the input of the MM fiber bundle. The concave surface is facing the incoming beam. The distances in the setup were 45mm between the lens and the MM fiber bundle input and 50mm between the focusing lens and the MM fiber bundle input.

The lens has been mounted in the setup in between the focusing lens and the input of the MM fiber bundle, at the distance that allowed the optimal coupling. Figure 4.1 shows a schematic representation of the setup when implementing the lens during the beam characterization phases.

4.2 Software correction

To correct for the intensity fluctuations, in particular along time, additional steps in signal processing have been implemented.

- Frame Averaging. After performing image reconstruction of the raw OA data through the back-projection algorithm, the 3D volumes of OA data have been further divided in subsets according to the correspondent wavelength. In this way, it is possible to separate the spectral information.
  In order to correct the presence of outliers and possible artifacts, frame averaging is performed selecting a number of consecutive reconstructed volumes and averaging their value. In this case, 10 consecutive frames were selected and their volumetric information averaged.

Chapter 5

Results

Synopsis This Chapter reports the results obtained during the experimental studies described in Chapter 3, applying the corrections described in Chapter 4.

Section 5.1 shows the results obtained during the first experimental tests, aimed to characterize the illumination profile at the beam source and the target interface and evaluate its spatial and temporal changes.

Section 5.2 reports the results obtained performing OA imaging on agar custom-made phantoms, testing the corrections described in Chapter 4.

Section 5.3 reports the results obtained in the preclinical in vivo neuroimaging experiment with applied corrections.

5.1 Beam Characterization

In this Section are reported the results obtained in the first part of the experimental work, aimed to characterize the beam profile through the use of a PC-controlled camera. These results describe the initial nature of the beam behavior at the source and target interface.

Initial illumination profile

To analyze the illumination profile, the light distribution has been observed in different sites along its path.

At first, the beam profile was studied at the laser emission (Figure 5.1). Then, also illumination profile at the target interface was analyzed (Figure 5.2).

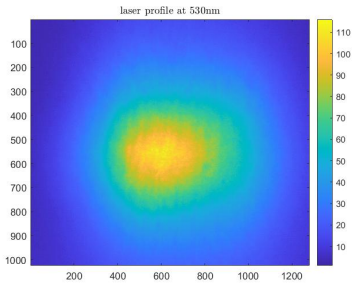

(A) beam profile at 530nm

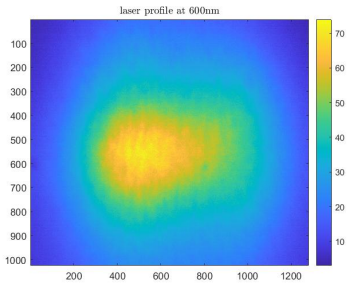

(B) beam profile at 600nm

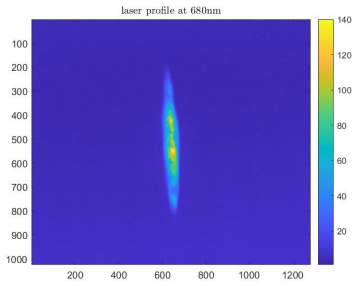

(C) beam profile at 680nm

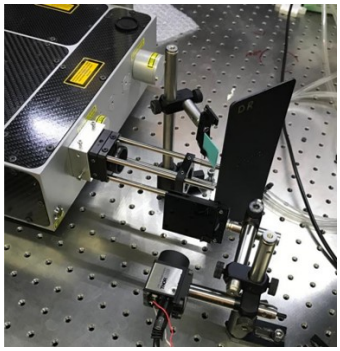

(D) Experimental setup

Figure 5.1: Characterization of beam profile at the source. (A), (B), (C) beam profile at 530nm, 600nm and 680nm respectively; (D) part of the experimental setup realized to record images of the beam profile.

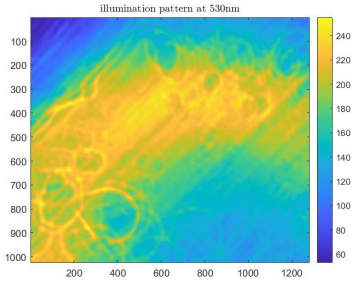

(A) wavelength 530nm

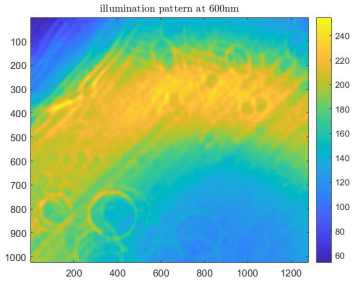

(B) wavelength 600nm

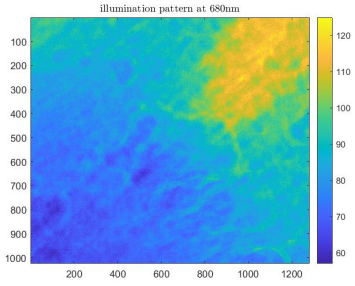

(C) wavelength 680nm

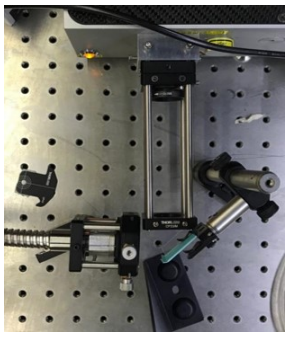

(D) Experimental setup

Figure 5.2: Characterization of beam profile at the target interface. (A), (B), (C) illumination profile at 530nm, 600nm and 680nm respectively; (D) part of the experimental setup used, showing beam coupling with the MM fiber input.

Table 5.1: Powermeter acquisitions of laser energy at the source recorded at the three different wavelengths.

λ(nm)	530	600	680
min. energy (mJ)	11.7	10.2	15.6
max. energy (mJ)	13.6	12.0	23.9
mean energy (mJ)	12.9	11.9	19.9
std (μm)	244	272	1090

Here the camera is able to acquire the light distribution that generally showcases onto the tissue under investigation.

The investigation along the different beam distances has been conducted always at three different wavelengths, two in the visible and one in the NIR range. sa

Thanks to the use of a powermeter it was possible to measure the energy output of the free laser beam and evaluate the energy fluctuations present at the origin at each of the employed wavelength (Table 5.1). The values recorded show similar ranges for the two wavelengths used on the visible laser (530nm and 600nm); instead, when illuminating at 680mn from the NIR laser, higher energy fluctuations are recorded, demonstrated by the peak value in the temporal std.

After acquiring the images through the use of the PC-controlled camera, the data have been processed on Matlab to extract statistical parameters relative to the laser behavior in time and space.

The temporal standard variation has been computed on the beam profile at the source and the target interface, comparing the different wavelengths used during the experiment (Figure 5.3). The results reported are computed on normalized intensities. The original intensity range (0-255) acquired from the camera has been scaled to 0-1 to allow comparisons.

From the plots, it is possible to notice how the temporal std appears different according to the used laser: when illuminating the system using the visible laser, the temporal std at the source oscillates around higher values, and it decreases along the optical path to the target. An opposite behavior can be seen when using the NIR laser, where the temporal std at the source was around smaller values.

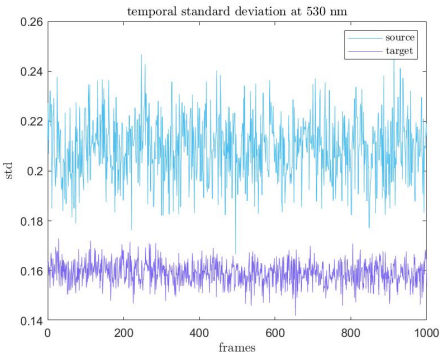

(A) wavelength 530nm

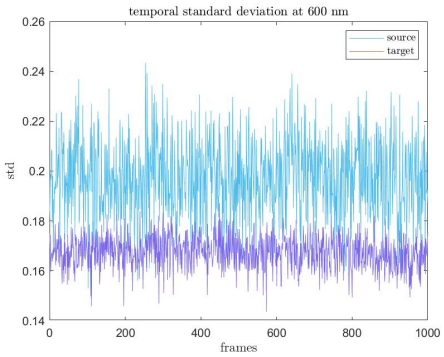

(B) wavelength 600nm

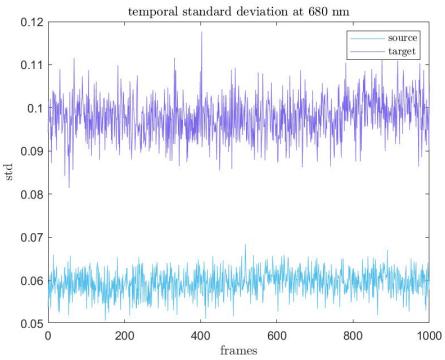

(C) wavelength 680nm

Figure 5.3: Temporal standard deviation of beam profile acquired with the Thorlab camera. Comparison betweed std oscillations at the source and at the target interface.
(A), (B), (C) temporal std at 530nm, 600nm and 680nm respectively.
The results reported are computed on normalized intensities. The original intensity range (0-255) acquired from the camera has been scaled to an unitary range (0-1) to allow comparisons.

Along with the temporal analysis, also a spatial analysis has been carried out in order to investigate the behavior of the free beam and of the illumination profile in the system.

The behavior of each pixel as a function of time can be characterized using its standard deviation, which enhances the differences on the illumination pattern.
The same time analysis has been computed on the dataset acquired at the illumination source (Figure 5.4), and similarly on the one acquired at the target interface (Figure 5.5).

Additionally, also the histogram plots of the spatial standard deviation for the illumination profile at the target interface have been reported (Figure 5.6). The

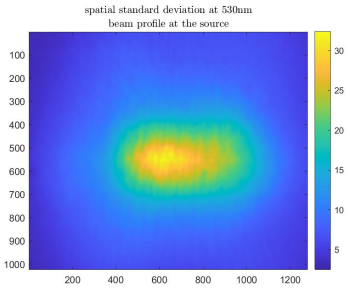

(A) wavelength 530nm

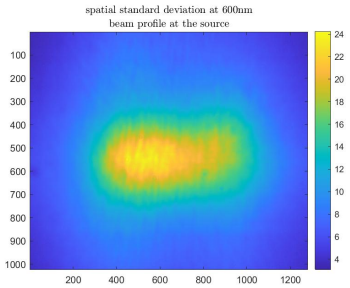

(B) wavelength 600nm

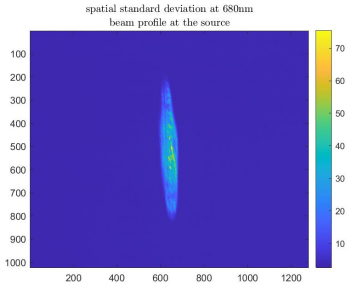

(C) wavelength 680nm

Figure 5.4: Spatial standard deviation of beam profile at the source.

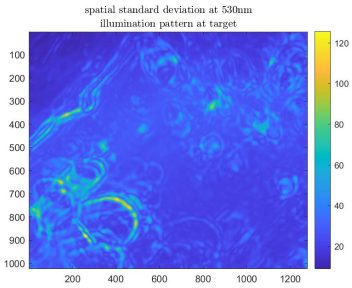

(A) wavelength 530nm

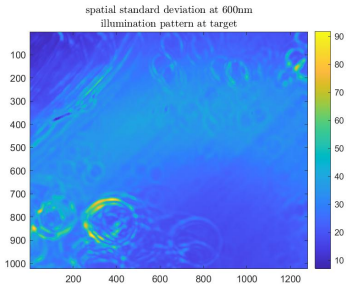

(B) wavelength 600nm

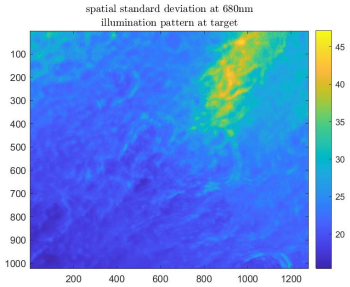

(C) wavelength 680nm

Figure 5.5: Spatial standard deviation of beam profile at the target interface.

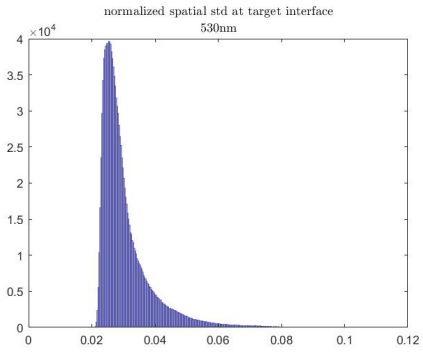

(A) wavelength 530nm

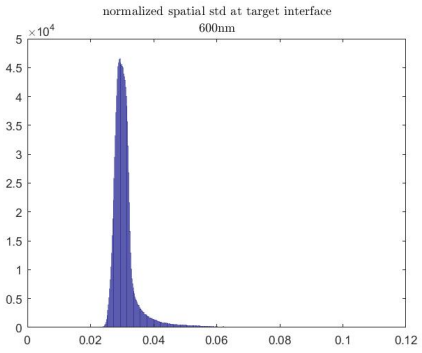

(B) wavelength 600nm

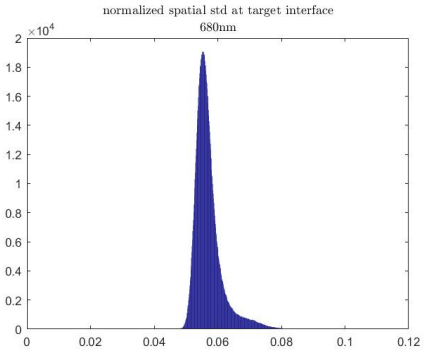

(C) wavelength 680nm

Figure 5.6: Histogram of normalized spatial standard deviation of beam profile at the target interface. The normalization has been obtained using a reference image from the batch of acquisitions

histograms contain the information relative to the normalized dataset, i.e. after selecting one image from the batch of acquisition as a reference image to perform the normalization procedure as described in Chapter 3.

Degassed water

In this section are reported the results obtained implementing the fluctuations corrections described in Chapter 4.

In particular, the results shown here refer to the use of degassed water and additional filtering/cleaning of the optical components in the setup.

2D camera acquisitions of the illumination profile at the target interface have been performed, both using degassed DI water as coupling medium (Figure 5.7), and using

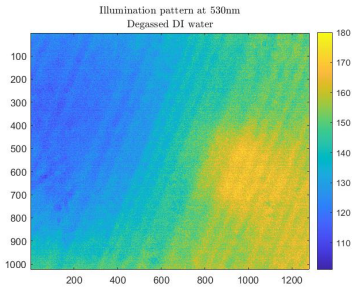

(A) wavelength 530nm

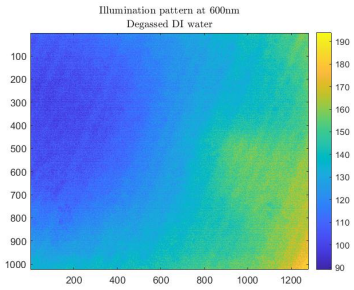

(B) wavelength 600nm

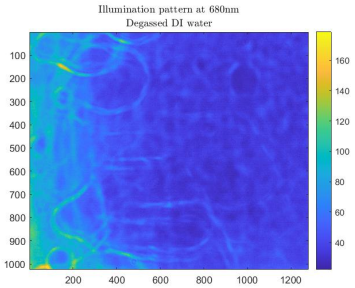

(C) wavelength 680nm

Figure 5.7: Results of illumination profile employing degassed DI water on the setup. (A), (B), (C) illumination profile at 530nm, 600nm and 680nm respectively.

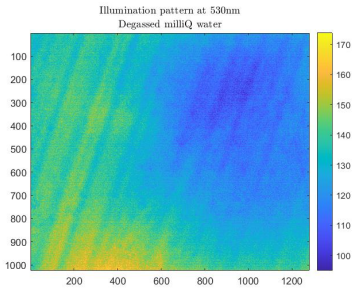

(A) wavelength 530nm

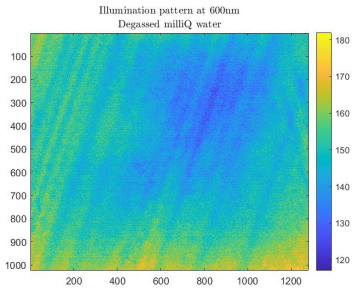

(B) wavelength 600nm

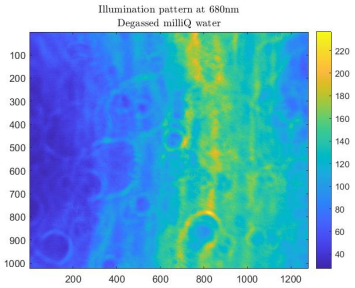

(C) wavelength 680nm

Figure 5.8: Results of illumination profile employing degassed milliQ water on the setup. (A), (B), (C) illumination profile at 530nm, 600nm and 680nm respectively.

degassed milliQ water (Figure 5.8).

After visually checking the uniformity of the illumination pattern in the new setup, the data have been analyzed in order to extract the statistical parameters and have a quantitative comparison with the previous setups.

Temporal std has been computed in all the dataset, and compared according to the investigative wavelengths (Figure 5.9).

To further understand the effect of light coupling on the final illumination pattern, Table 5.2 reports the expected speckle sizes computed according to the wavelength, a fixed distance of 4cm between the surface of the major output tail, and 179 μm

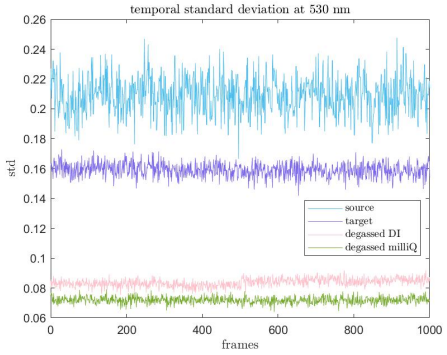

(A) wavelength 530nm

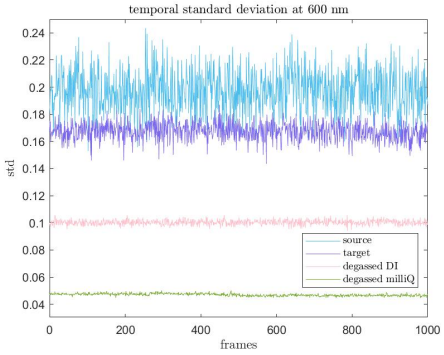

(B) wavelength 600nm

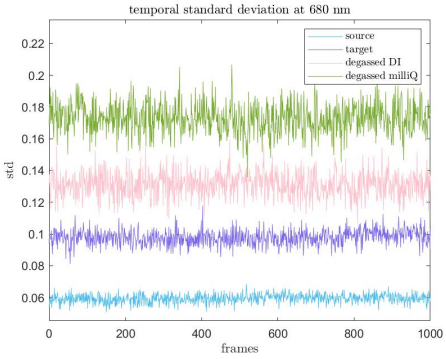

(C) wavelength 680nm

Figure 5.9: Comparison betweed temporal standard deviation oscillations at the source, at the target interface using DI water, and at the target using degassed DI water and degassed milliQ water. (A), (B), (C) temporal std at 530nm, 600nm and 680nm respectively. The results reported are computed on normalized intensities. The original intensity range (0-255) acquired from the camera has been scaled to an unitary range (0-1) to allow comparisons.

Table 5.2: Speckle size estimation. Expected speckle size (Ss) has been computed using the formula $Ss = \lambda \cdot z \cdot \frac{1}{D}$, where z = 4cm is the distance between the face of the MM fiber main output tail, D = 179μm is the beam diameter and λ refers to the employed wavelength. [47]

λ (nm)	Ss (μm)
530	118.43
600	134.08
680	151.95
730	163.13
755	168.71
800	178.77
850	189.94

beam diameter as specified in the MM fiber bundle technical report.

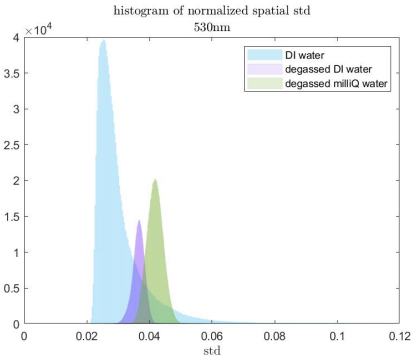

(A) wavelength 530nm

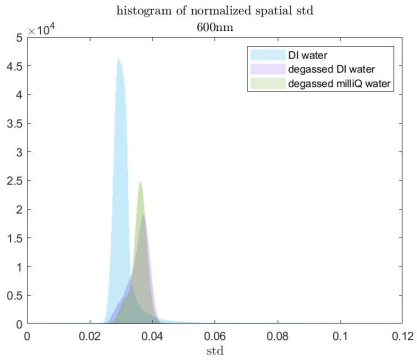

(B) wavelength 600nm

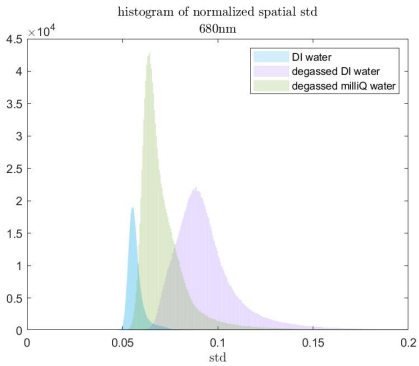

(C) wavelength 680nm

Figure 5.10: Histogram of normalized spatial standard deviation of beam profile at the target interface using different coupling medium (DI water, degassed DI water and degassed milliQ water). (A), (B), (C) temporal std at 530nm, 600nm and 680nm respectively. The normalization has been obtained using a reference image from the batch of acquisition.

Eventually, Figure 5.10 reports a comparison of the histograms of normalized spatial deviation computed on the different datasets. In particular, the comparison has been made between the various medium that is possible to employ in the setup, i.e. DI water, degassed DI water, and degassed milliQ water.

Optical correction

In order to obtain a rounder beam profile when using the NIR laser, the optical correction described in Chapter 4 has been implemented and compared.

The 2D images were acquired using the camera. The illumination pattern at the target interface was recorded when using DI degassed water and a plano-concave cylindrical lens, able to expand the beam monodirectionally (Figure 5.11).

To compare the spatial distribution with the previous data acquired at 680nm, also the histogram of the normalized spatial standard deviation has been computed, achieved using one random image from the dataset for the normalization.

Thus, Figure 5.12 reports a comparison between the histograms obtained from the initial dataset with the original NIR beam shape, and the results obtained when implementing both optical correction and degassed water.
In particular, for the latter, degassed DI water has been used, together with the

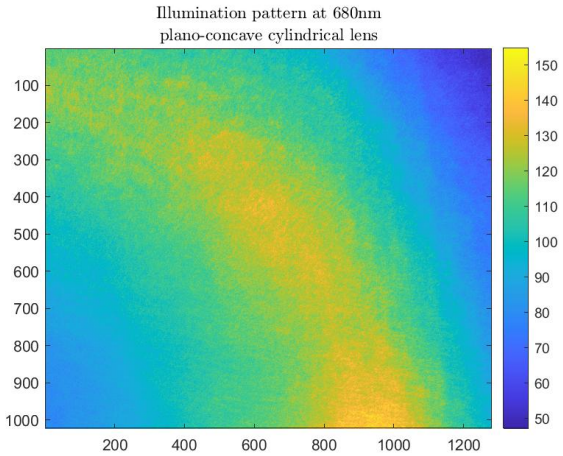

Figure 5.11: Illumination pattern at the target interface at 680nm with optical correction acquired with the camera. To correct the beam a plano-concave cylindrical lens with focal distance f=-6.35 mm (Thorlabs, Inc.) has been used.

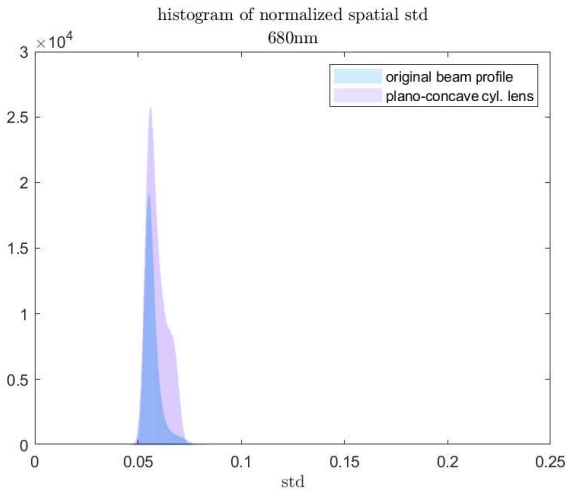

Figure 5.12: Histograms of the normalized spatial standard deviation of beam profile at 680nm at the target interface between original acquisition and optical correction achieved through a plano-concave cylindrical lens. The normalization has been obtained using a reference image from the batch of acquisitions. The 2D images were acquired through the camera. std at peak values coincide at 0.06 for both dataset.

plano-concave cylindrical lens to correct the beam shape.

To evaluate the temporal behavior of the illumination pattern in presence of the optical corrections, 4 different regions have been selected in order to compute temporal correlation as described in Chapter 3.

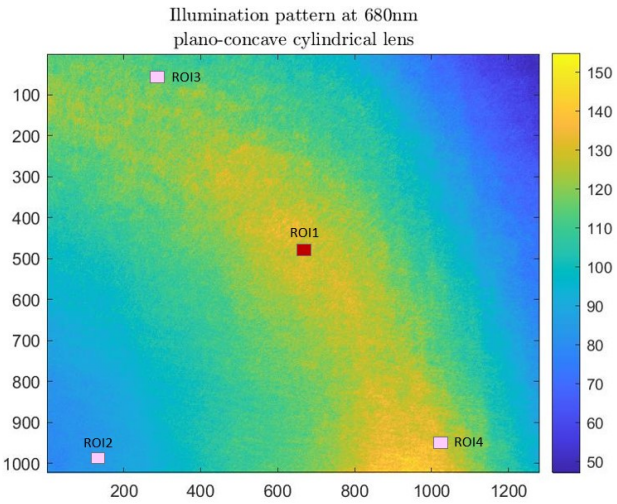

Figure 5.13: Selection of ROIs from one reference 2D image in the batch of acquisition done through the camera at target interface at 680nm with optical correction. ROI1 has been selected in the central region of the image; ROI2, ROI3, ROI4 have been selected in peripheral areas as shown in the image.

Table 5.3: Results of temporal correlation computed in selected ROIs from illumination at target interface at 680nm with optical correction.
The table reports the results of ROI1 with ROI2, ROI3 and ROI4 respectively. The values have been computed as average intensity registered in the pixels in the selected area for each instant of time.
Normalization has been performed using one reference image form the original batch of acquisition.

ROI	ρ
ROI2	0.9978
ROI3	0.9920
ROI4	0.9987

Figure 5.13 shows the pixels selection. ROI1 has been chosen in the central area, where usually biological information is present; on the other hand, ROI2, ROI3, ROI4 have been chosen on peripheral areas, to be possibly used as a reference to evaluate laser fluctuations.

In Table 5.3 are reported the results for the temporal correlation, computed between the intensity of ROI1 along time, and the values for ROI2, ROI3, and ROI4 respectively.

5.2 Phantom

After testing the corrections on the setup and evaluating the linked outcomes, additional tests have been performed using OAI. In this section are reported the results obtained using phantoms to test the system response.

To compare the efficiency of the optical correction, the data were acquired once with the original setup and then with the implementation of the optical correction. The chosen medium is degassed DI water for both setups.

In particular, the reported figures show the acquisitions done at 850nm.
The results for the other exploratory wavelengths were consistent with the shown one, thus are not reported.

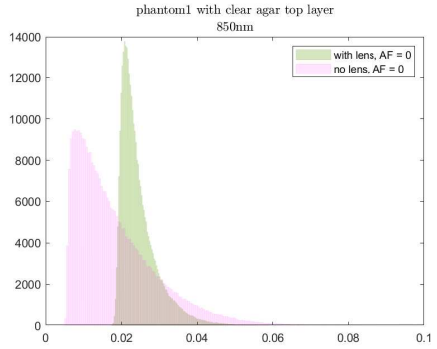

(A) phantom with ink concentration 0.1%, clear agar top layer

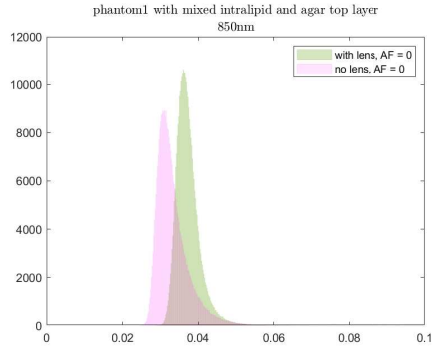

(B) phantom with ink concentration 0.1%, mixed intralipid and agar top layer

Figure 5.14: Comparison of histogram of normalized spatial standard deviation in OA images of homogeneous phantoms acquired with and without optical correction.
(A) results relative to phantom with 0.1% ink concentration and clear agar top layer;
(B) results relative to phantom with 0.1% ink concentration and mixed intralipid and agar top layer.
The normalization has been obtained using a reference volume from the batch of acquisitions.

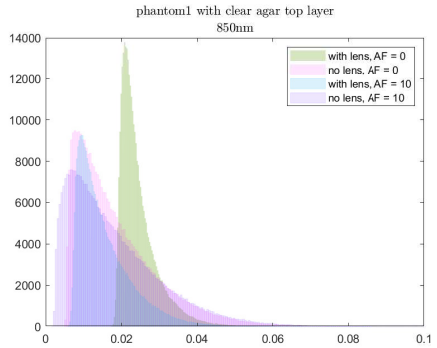

(A) phantom with ink concentration 0.1%, clear agar top layer

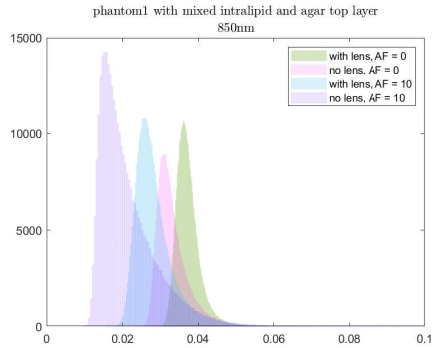

(B) phantom with ink concentration 0.1%, mixed intralipid and agar top layer

Figure 5.15: Evaluation of frame averaging software correction.
Comparison of histogram of normalized spatial standard deviation in OA images of homogeneous phantoms acquired with and without optical correction, with (FR = 10) and without (FR = 0) performance of frame averaging on 10 consecutive frames acquired at the same wavelength.
(A) results relative to phantom with 0.1% ink concentration and clear agar top layer;
(B) results relative to phantom with 0.1% ink concentration and mixed intralipid and agar top layer.
The normalization has been obtained using a reference volume from the batch of acquisitions.

Table 5.4: Std values at distribution peak in phantoms acquisitions.

	clear agar	mix intralipid
AF=0, with lens	0.021	0.037
AF=0, no lens	0.009	0.031
AF=10, with lens	0.010	0.026
AF=10, no lens	0.007	0.015

In the reported results is possible to see the comparison of the distribution of the spatial standard deviation.

More precisely, Figure 5.14 (A) reports the results relative to OA images acquisition of the phantom made with ink concentration of 1% made with a clear agar superficial layer.

Figure 5.14 (B), on the other hand, shows the results relative to the second phantom, with the same ink concentration, but a superficial layer made with a mixed composition of agar and intralipid.

Figure 5.15 reports the results for the frame averaging correction, performed as described in Chapter 4, on the 3D volumes relative to OA images of the phantoms. Relative quantification of std values at the peak of the distribution is reported in Table 5.4.

5.3 In vivo

To investigate and compare the benefits of the hardware and software modifications applied, OA mouse neuroimaging was performed in vivo.

After performing MSOT on in vivo mouse brain, the data have been reconstructed by means of the universal back-projection algorithm, with adjusted speed of sound SoS = 1485 m/s, and filtered to reduce the presence of unwanted noise.

In particular, cutoff frequencies were applied at 2 MHz (low cutoff frequency) and 8 MHz (high cutoff frequency). Additional 3D filtering has been performed by applying a brain mask filter, created based on anatomical mouse brain atlas.

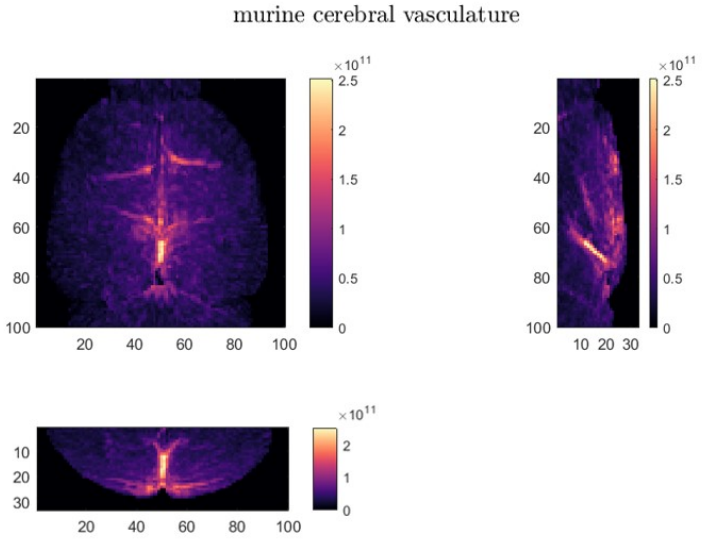

Figure 5.16: In vivo OAI of murine cerebral vasculature at coupling distance d1.
Top left shows frontal view of the mouse brain; top right lateral view, and bottom figure displays in-depth view. The visualization is obtained by displaying MIPs.

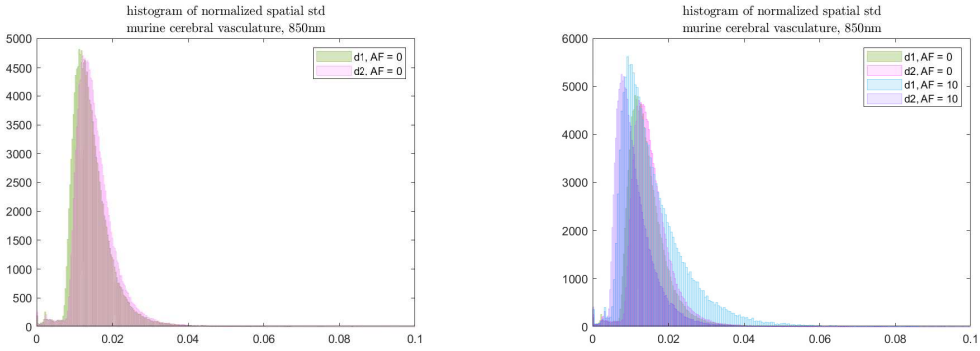

(A) comparison at different coupling distances without frame averaging

(B) comparison at different coupling distances with and without frame averaging

Figure 5.17: Evaluation of software and hardware corrections on in vivo results of OA mouse neuroimaging.
Comparison of histogram of normalized spatial standard deviation for in vivo results of OA mouse neuroimaging, acquired at 850nm. Optical correction was achieved through closer coupling position (d1 < d2). Software correction was performed with (AF = 10) frame averaging on 10 consecutive frames acquired at the same wavelength and without (AF = 0).
(A) only results relative to the optical correction are shown; (B) comprehensive comparison of hardware and software results.
The normalization has been obtained using a reference volume from the batch of acquisitions.

Table 5.5: Std values at distribution peak in in vivo acquisitions.

	d1	d2
AF=0	0.011	0.014
AF=10	0.008	0.010

In this way, it was possible to discriminate between the anatomical voxels and the ones laying outside of the cerebral structures.

After applying hardware and software corrections, it is possible to clearly display the main vessels and cerebral structures (Figure 5.16). Employing degassed DI water guaranteed the absence of local spots of high fluence and inhomogeneities, allowing clear visualization of hemodynamic processes. It should be noted, however, that the purpose of this work did not concern the monitoring of hemodynamic changes due to external stimulations, thus only a reference frame from the batch is reported for illustrative purposes.

The results of different coupling efficiency were compared before (Figure 5.17 (A)) and after (Figure 5.17(B)) frame averaging. Relative quantification of std values at the peak of the distribution are reported in Table 5.5.

To reach further insights on the spatial std, the volumes were investigated by displaying frontal and lateral maximum intensity projections (MIPs), comparing the results with and without hardware and software corrections (Figure 5.18).

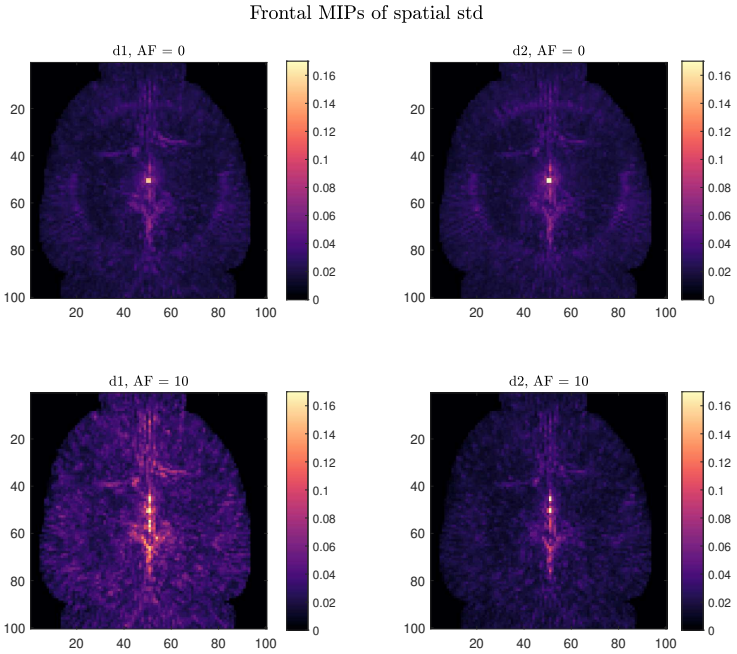

(A) Frontal display of MIPs of spatial std with and without corrections

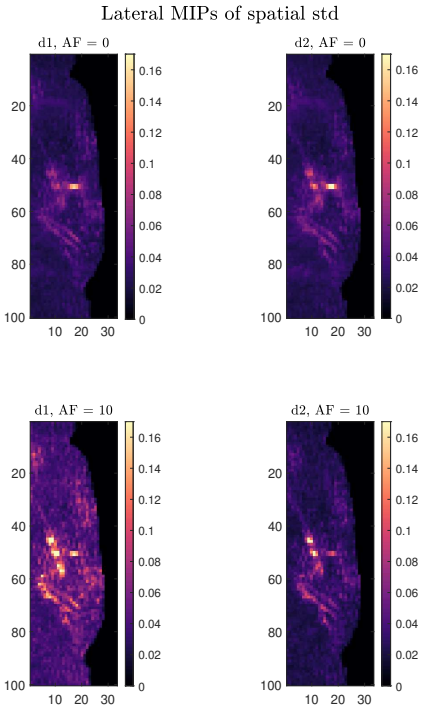

(B) Lateral display of MIPs of spatial std with and without corrections

Figure 5.18: (A) Frontal and (B) lateral MIPs display of spatial std of in vivo OA mouse neuroimaging performed with and without hardware and software corrections

Chapter 6

Discussion

Synopsis In this Chapter, the results presented in Chapter 5 are analyzed and discussed, starting from the observations based on the *2D camera* acquisitions, up to the results of OA *phantoms* and *in vivo* imaging data.

OAI relies on powerful short laser pulses to trigger thermal expansion in the target chromophores and image the tissues. In order to understand the nature of the optical beam that plays such a fundamental role in the technique, various steps have been followed during the investigative quest.

At first, the laser illumination profile has been studied at the beam source and the target interface, exploring three different wavelengths. Employing a camera, it has been possible to acquire 2D images of the beam profile and compare them.

Already at the laser emission, the beams appear to be different according to the exploratory wavelength employed (Figure 5.1). In fact, it is possible to notice that the beam profile at visible wavelengths shows a more homogeneous rounder shape, with respect to the mainly vertical shape that characterizes the 680nm beam.

However, it should be noted that two of the three datasets belong to the VIS laser (530nm and 600nm), while the last one (680nm) is of the NIR laser.
Indeed, being the lasers two actual different devices, operating in two different wavelengths ranges, it is not unlikely that some physical differences are present in the

construction systems of the lasers themselves. Such differences play a major role in determining the shape of the beams, due to the combination of the inside mirrors that shape the final beam that is released.

After investigating the source, also the final illumination pattern has been studied. It is certainly important to know what is the initial light profile when setting up the system, but eventually what is actually in contact with the target tissue to be visualized is the light distribution at the end of the optical path.
Once more, through a camera, it has been possible to acquire 2D images relative to the light distribution at the target interface, where the illumination pattern does not look homogeneous (Figure 5.2).
After traveling through the fibers and the water, photons create a distribution at the target interface which affects the uniformity of the final images. In particular, what is possible to detect from the 2D acquisitions, is the presence of microbubbles in the system. As they result not being fully transparent to water, their presence becomes noxious to the results of the imaging modality. Thus, preventing their presence might definitely result helpful to improve the acquisitions' stability.

After investigating the spatial distribution of the laser beam, also its energy and temporal behavior have been taken into account. Through the use of a powermeter, it has been possible to record the energy fluctuations simultaneously to the camera acquisitions (Table 5.1). Again, it is possible to detect differences related to the used wavelengths. While the energy recorded slightly decreases between the beam at 530nm and 600nm, the std computed is of similar value, showing a similar temporal behavior for the beams emitted from the VIS laser. On the other hand, the laser beam at 680nm results to carry higher energy within itself, and at the same time be more subjected to temporal fluctuations in energy.
By analyzing the energy variations, it is possible to understand that light intensity is not constant over time, rather it changes among a quite spread range of values from pulse to pulse, giving birth to temporal fluctuations.

To have further insights on the nature of the beam fluctuations, statistical parameters have been computed. At first, the temporal std has been computed from both

the 2D images batch acquired at the source and the target interface (Figure 5.3).
It is interesting to notice how the temporal std appears different according to the used laser: the std is greater in value and fluctuations when computed at the source in the VIS wavelengths, while it results smaller in the NIR acquisition. Instead, the difference decreases among the three datasets when the temporal std is computed at the target interface, with the lowest values being still related to 680nm.
The temporal standard variation is a useful parameter to monitor the spatial variations along time. Each sample represents the std computed in one 2D image at one time instant. The lower the value, the most homogeneous the image, hence, in this case, the illumination pattern. Having an increase in the values computed at the target could be explained by looking at the illumination patterns (Figure 5.1 and Figure 5.2): when studied at the source, the illumination pattern is characterized by a focus in the central area of the image, whereas the pixels confined at the peripheral areas show very low intensity; instead, the range of different illumination intensity is smaller in the illumination at the target, with pixels assuming all different intensities. By comparing the images of the raw beam, it is possible to notice how for the VIS laser the high-intensity pixels are more spread over the 2D plane, while in the NIR laser they are confined in a minimal region, with almost null intensity pixels taking over the majority of the area.

By plotting the spatial std instead, it is possible to investigate the temporal behavior of each pixel. It is possible to notice how the pixels that change the most their intensities along time are the ones with the highest intensities; that shows how the presence of "hotspots", i.e. points in space where the light hits with the highest strength, is particularly inconvenient for OAI. It causes biased light illumination, moreover not consistently in time, causing the presence of single artifacts difficult to detect and remove.
When investigating the beam at the source (Figure 5.4), the pixels characterized by the highest std lie at the center of the beam, while it is interesting to notice how at the target interface (Figure 5.5) they follow mostly circular shapes. Most likely, the presence of impurities and unwanted air inside the medium, namely microbubbles, affects the light path, creating shadows and illumination inhomogeneity on the target. Moreover,

microbubbles also appear to float in the medium, adding additional time-variant noise.

Additional insights are provided by the computation of the histogram of the normalized spatial std (Figure 5.6). Following the normalization procedure described in Section 3.5, the plot can describe the intensity variation that affects the beam along time. The narrower the histogram shape, the most similar the pixels' std computed along time. Hence, the most spatially homogeneous the images.

After performing beam characterization on the initial conditions of the system, different hardware alternatives have been implemented, to achieve a more uniform and stable illumination profile.

First of all, to solve the problem of unwanted presences inside the coupling medium with which the USD cup is filled, filtering methods have been implemented as described in Section 4.1. Therefore, it has been possible to assure the absence of the majority of microbubbles and impurities that affected the initial setup. Such result is visually proven by the 2D images acquired at the target interface (Figure 5.7 and Figure 5.8): the illumination profile at 530nm and 600nm appears more uniform, and most importantly, it does not result affected by bubble-like shapes as it was initially.

However, it is still possible to notice the presence of some shapes. The vertical lines that can be seen, are most likely due to the transparent film used to seal the USD cup; in addition to this, other reflections can be seen in the images acquired at 680nm. Given the different results between the two used lasers, the fact that the medium composition has not been changed between the different wavelengths acquisitions, the differences in the results might be explained by referring to the original beam shape.

Figure 5.9 reports the results for the temporal std computed in the newly acquired datasets: as it is possible to see, the values relative to the acquisitions at the VIS wavelengths decrease with respect to the initial acquisition at target interface done using non-degassed DI water. On the contrary, contrasting results are obtained for the acquisition at 680nm, where the temporal std appears to increase, presumably due also to the inhomogeneity of the illumination distribution.

Thus, to explain the presence of such a pattern, it is helpful to think about the entire optical path: in OA neuroimaging, light travels from the laser output through the MM fiber bundle and exits within the USD cup internal volume from 4 different locations. Assuming that the water contribution to the illumination variation in time and space can be reduced by preventing microbubbles and impurities in the system through the use of filtering methods, what occurs at the interface appears to be mainly linked to what happens to the beam at the coupling interface.

Therefore, the original beam shape plays an important role: to couple the entire beam, its shape should match the circular input of the MM fiber. It is possible to notice how while this could be easily achieved for the VIS laser, which originates a quite round beam, it becomes tricky when dealing with the NIR laser, due to the singular shape of the beam. From the definition of the coupling coefficient itself, the number of fibers that correctly couple the light is proportional to the relation between the beam size and shape, and the fiber input. The highest coupling coefficient is ideally obtained when dealing with a gaussian beam, which, as a matter of fact, has an axial round and symmetrical shape [46]. Having a vertical beam does not allow to couple all the fibers in the same way, which results in optimal coupling for the fibers located along the main axis of the beam, and almost null contribution from the marginal ones. The fibers are then regrouped along with the bundle, eventually leading to an illumination surface affected by hotspots and "speckle" pattern, due to the differences in the contribution of the fibers.

To further understand the light speckle effects, expected values of their size according to the system's characteristics have been computed (Table 5.2). It is possible to see how the expected size increases according to the wavelength, starting from a size of around 100 μm, which already corresponds to modern OAI systems' spatial resolution.

Eventually, to conclude the evaluation of the spatial uniformity achieved with the filtering and degassing method, histogram plots of the normalized spatial standard deviation have been compared (Figure 5.10). Once again, distinctions must be made according to the used laser. When operating the VIS one, it is clear that the distributions obtained when using degassed water are narrower than the one relative to using normal DI water, suggesting that the spatial fluctuations are actually reduced

thanks to the filtering procedures.

Moreover, among the two different degassed water qualities tested in the VIS illumination, DI appeared to be a better choice, mainly for two reasons: first, the illumination profile appears to be more homogeneous when compared to the one obtained using milliQ water, as confirmed by the narrower histogram; in addition, milliQ water is not trivial to obtain as it requires more specific filtering and purification techniques to be made, while DI water is more easily available for experimental purposes.
Despite this, the dataset acquired at 680nm reports contradictory results, as distributions related to using degassed water appear to be even wider. Once again, the difference in the initial profile of the free beams is to be blamed.

Thus, considering the shape of the beams, along with all the previously described results, it appears to be that spatial fluctuations still present, if not even increased, in the NIR illumination pattern, might be mostly related to the non-optimal coupling between the free beam and the MM fiber bundle input. For this reason, optical hardware corrections have been tried, in order to improve the initial coupling and avoid biased photons transmission.

To expand the beam monodirectionally, achieving a more round and symmetrical shape, a plano-concave cylindrical lens has been used. Figure 5.11 shows the illumination pattern resulting at the target interface. Comparing it with the previous results of illumination profiles at 680nm, the images of the illumination pattern obtained when using the lens appear to be less affected by light inhomogeneities, allowing a more uniform final illumination profile, almost speckle-free.

Figure 5.12 reports the histograms of the normalized spatial std. Unexpectedly, the plot for the dataset with both optical correction and water filtering doesn't show improvements compared to the one obtained in the initial setup with normal DI water, as the distributions appear to be of comparable width. However, when comparing with the dataset related to degassed water without the optical correction implementation (Figure 5.10), the result from the acquisitions performed with both hardware corrections shows largely improved results .

To test the temporal behavior of the pixels, the temporal correlation has been computed as described in Chapter 3. Figure 5.13 shows the choice of the ROIs from one reference image in the datasets acquired at the target interface at 680nm with optical correction. The results for the analysis, reported in Table 5.3, show incredibly high correlation coefficients. This means that the temporal fluctuation to which one region's intensity is affected over time is almost perfectly linearly correlated with the variation in another ROI, in this case, the central selected area.

After testing the corrections performed on the optical path, the effects of the hardware setup optimization have been tested in full OA modality. Given the way the OAI system is built, the images of the target were acquired through the creation of US waves from the absorbing particles. Thus, the 3D volumes obtained after reconstruction are proper of the composition of the phantoms themselves and are not able to analyze directly the illumination profile at the target interface.

OAI abilities in imaging deeper structures rely on the choice of longer wavelengths: especially in neuroimaging, wavelengths in the NIR ranges are mostly used. Hence, evaluation of the laser fluctuations in OAI was performed using the NIR laser and comparing the histogram of normalized spatial std acquired with full hardware correction, and without the lens, i.e. maintaining the initial coupling of the free beam with the MM fiber bundle input.

As it is possible to see (Figure 5.14), when imaging the phantom with a clear agar top layer, the distribution relative to the fully corrected setup appears to be narrower than the one without optical correction. Nevertheless, when imaging the phantoms with the top layer made of mixed agar and intralipid, it is not possible to detect a marked improvement, as the width of the distributions appears to be much similar.

The purpose of using a mixture of intralipid in the top of the phantom, however, was to create a scattering layer to mimic the skin and observe similar results to what happens to tissue-light interaction when imaging in vivo. Thus, biologically speaking, the similar distribution of the histograms in Figure 5.14(B) shows that the lens improvements are quite lost along with the scanning depth of the target, as the

skin acts as a diffuser making light distribution more homogeneous.
Hence, the lens improvements mostly benefit imaging at superficial levels, where the choice of the wavelength relies only on the molecules that one wants to investigate, according to their proper absorption coefficient.

Furthermore, a remark must be made on the value of the std assumed by the peak of the distributions (Table 5.4). With the optical correction, in fact, the distributions narrow, but also shift to the right towards higher std values. The increase in the value of the std, reflects a wider distribution in terms of temporal fluctuations of the considered voxel. One explanation for such increase might be found in the use of the lens itself, which affects the amount of energy delivered to the target and thus the final SNR. For this reason, the signals result affected by an increased presence of random noise, which determines the raise in std.

Additionally, corrections for the temporal fluctuations in OA have also been tested. By implementing frame averaging as described in Section 4.2, the distribution represented by the histogram appears to be shifted towards lower values (Figure 5.15). That represents an improvement on the temporal point of view, as it means that the standard variation of the intensity of the voxels along time shows a less spread out range, hence the values of intensity assumed by that same voxel along time are more similar to each other (quite constant in time). That was actually expected, as by performing averaging of the temporal volumes it is possible to reduce the presence of outlier values, and so somehow correct for artifacts and temporal variations.
Despite the achievement, it is important to take into account that by performing frame averaging the temporal resolution lowers: when imaging in vivo, this translates into losing the ability to detect ultra-fast events happening in the brain, such as some neural coupling mechanisms. Thus, a compromise should be made between the level of fluctuations that could be tolerated and the temporal resolution needed to correctly visualize the brain mechanisms.

To check the uniformity of the temporal behavior of the voxels, the temporal correlation has been computed on frame averaged 3D volumes, normalized by a reference volume. Unexpectedly, the ρ values computed show all almost null values,

indicating the absence of a linear correlation among voxels intensity along time. This result is in contrast with what was obtained from the camera acquisition, where the linear correlation was almost 1.
The reason for this absence of correlation might be linked to the reconstruction algorithm, which might cause the loss of linear correlation among different regions in the target volume, especially when affected by low SNR, as it happens when implementing optical corrections.

For this reason, additional analysis of the beam profile along its axis of propagation has been performed. It was possible to identify the beam as astigmatic, i.e. a beam whose focal points for the vertical and horizontal direction do not coincide.
However, given the geometry of propagation of the NIR laser beam, it is possible to identify a region of its profile where it appears quite symmetrical, and not as vertical as in the distal range.
As known, the shape of the beam section at the coupling interface greatly influences the coupling efficiency [46]. In the previous setups, the optimal coupling position was identified as the one where the maximum energy was delivered to the target, no matter the profile at the coupling interface (d2). In the new setup instead, a different coupling distance was defined, i.e. the one where the beam profile appeared the most symmetrical and matched the round section of the MM fiber bundle input (d1).
In this way, it was possible to achieve the same coupling effect as when using the concave cylindrical lens, but without loss of energy due to the beam crossing the lens.

Thus, it was possible to couple the light beam equally among the fibers at the input of the MM fiber bundle avoiding a major loss in the SNR.

The effects of different coupling positions have been tested on full OAI of in vivo mouse brain (Figure 5.17). It is already possible to notice from the anatomic reconstructed image, that the employment of filtering methods prevents the formation of microbubbles and local high fluence spots, allowing clear visualization of hemodynamic processes (Figure 5.16).

As far as optical corrections are concerned, slight improvements can be seen in the data acquired at coupling distance d1, as represented by the std values at peaks of the distributions of the spatial std (Table 5.5), supporting the idea that a higher coupling coefficient allows a more homogeneous illumination.

Moreover, the small difference in distribution and peak-std value could also be due to damage on the input of the MM fiber bundle verified just before the experiment, which most likely prevented a homogeneous light coupling among the fiber, thus altering the final results with biased modes transmission.

In addition, it is still possible to notice that the difference between the value of the std of the two datasets decreases, compared to the greater difference showcased in the phantom acquisitions (Figure 5.14). Such reduced difference might be explained in the similar amount of energy delivered to the target in the two coupling distances, hence maintenance of similar SNR.

When performing frame averaging, it is possible to notice how the peak of the distribution shift towards lower std values (behavior consistent with the results of OAI of phantoms), as the presence of outliers is reduced by the algorithm. Once again the broadening of the distribution indicates a different temporal behavior across the reconstructed volumes.

Indeed, the presence of ongoing biological processes and hemodynamic changes make it difficult to interpret the results and enhance the differences just from the histogram plot of normalized spatial std. By displaying MIPs of std, it is possible to investigate more in-depth the nature of the std (Figure 5.18). It is quite clear that the use of frame averaging allows reduction of the ring-shaped reconstruction artifacts, clearly visible in AF = 0. However, the presence of focus artifact remains present in all reconstructed datasets, as one of the voxels characterized by the higher std. The ability of the frame averaging algorithm to correct for the ring artifact but not for the focus after reconstruction explains the broad shape of the histogram after software correction.

Furthermore, frame averaging allows increasing std in other voxels, depicting the major vessel. This fact might not represent a mere coincidence, but rather an effect

of biological changes due to brain activity.

Thus, by implementing frame averaging it is possible to get rid of random noise and reconstruction artifacts and at the same time enhance hemodynamic mechanisms in the vasculature, which are subjected to greater changes across time, due to ongoing biological processes.

Chapter 7

Conclusion and Future Work

This thesis addresses the problem that threatens the reliability of OA images, i.e. the fluctuations in laser-emitted light both in time and space.

By performing laser beam characterization, it was possible to understand how laser light strongly depends on each laser device's features. Moreover, given the complex setup for the imaging technique, the shape of the beam itself must be accurately characterized and corrected in order to allow a homogeneous illumination pattern onto the target.

The hardware corrections tested within this project proved to be valid allies in the assembly of OA neuroimaging setup.
In particular, water filtering and degassing allows strongly reducing the artifacts due to unwanted presences in the medium which cause spurious US signals, and also protecting the system from the danger of deterioration. In addition, optical corrections can be applied in order to achieve an optimal coupling coefficient and guarantee equal contribution by all the fibers to the final illumination, preventing speckle-pattern on the target.

The proposed hardware optimizations appear to be efficient to reduce the spatial fluctuations present in the light distribution at the target interface; this is also proved by the strong temporal correlation present among different ROIs randomly selected in the illumination surface.

Hardware corrections and additional software corrections through the frame averaging algorithm were tested also on OAI. By optimizing the coupling coefficient, the

results for the OA images of homogeneous targets showed improved spatial uniformity. In preclinical applications, that would improve the reliability of imaging of superficial structures, to which the photons are delivered with very little previous scattering.

When tested on the dataset acquired in vivo, frame averaging appeared to be one useful algorithm to reduce the presence of artifacts and random noises, without losing the information related to ongoing hemodynamic changes.

Despite the promising results on the 2D camera dataset, the temporal correlation was not as strong in OA reconstructed volumes, showing the nontrivial selection of meaningful ROI.

Future works could focus on testing a different kind of nonlinear temporal correlations, both in reconstructed and raw OA data, in order to find a reliable relation between the variations in intensity from pulse to pulse, and finally employ the intensity values registered in a marginal region as reference fluctuations with which correct for the central areas.

Bibliography

[1] B. Mc Larney, M. A. Hutter, O. Degtyaruk, X. L. Deán-Ben, and D. Razansky, "Monitoring of stimulus evoked murine somatosensory cortex hemodynamic activity with volumetric multi-spectral optoacoustic tomography," *Frontiers in Neuroscience*, vol. 14, 2020.

[2] J. Robin, R. Rau, B. Lafci, A. Schroeter, M. Reiss, X.-L. Deán-Ben, O. Goksel, and D. Razansky, "Hemodynamic response to sensory stimulation in mice: Comparison between functional ultrasound and optoacoustic imaging," *NeuroImage*, vol. 237, pp. 118–111, 2021.

[3] N. P. Blockley, V. E. M. Griffeth, A. B. Simon, and R. B. Buxton, "A review of calibrated blood oxygenation level-dependent (BOLD) methods for the measurement of task-induced changes in brain oxygen metabolism," *NMR in Biomedicine*, vol. 26, pp. 987–1003, aug 2013.

[4] S. C. Bosshard, C. Baltes, M. T. Wyss, B. Mueggler, T.and Weber, and M. Rudin, "Assessment of brain responses to innocuous and noxious electrical forepaw stimulation in mice using bold fmri," *PAIN§*, vol. 151, pp. 655–663, 2010.

[5] D. A. Yablonskiy, A. L. Sukstanskii, and X. He, "Blood oxygenation level-dependent (bold)-based techniques for the quantification of brain hemodynamic and metabolic properties – theoretical models and experimental approaches," *NMR in Biomedicine*, vol. 26, no. 8, pp. 963–986, 2013.

[6] L.-D. Liao, C.-T. Lin, Y.-Y. I. Shih, T. Q. Duong, H.-Y. Lai, P.-H. Wang, R. Wu, S. Tsang, J.-Y. Chang, M.-L. Li, and Y.-Y. Chen, "Transcranial imaging of functional cerebral hemodynamic changes in single blood vessels using in vivo photoacoustic microscopy.," *Journal of cerebral blood flow and metabolism :*

official journal of the International Society of Cerebral Blood Flow and Metabolism, vol. 32, pp. 938–51, jun 2012.

[7] J. F. Schenck, "The role of magnetic susceptibility in magnetic resonance imaging: Mri magnetic compatibility of the first and second kinds," *Medical Physics*, vol. 23, no. 6, pp. 815–850, 1996.

[8] T. Dill, "Contraindications to magnetic resonance imaging," *Heart*, vol. 94, no. 7, pp. 943–948, 2008.

[9] N. K. Logothetis, "What we can do and what we cannot do with fMRI.," *Nature*, vol. 453, pp. 869–78, jun 2008.

[10] F. Darvas, D. Pantazis, E. Kucukaltun-Yildirim, and R. Leahy, "Mapping human brain function with meg and eeg: methods and validation," *NeuroImage*, vol. 23, pp. S289–S299, 2004. Mathematics in Brain Imaging.

[11] A. T. Eggebrecht, S. L. Ferradal, A. Robichaux-Viehoever, M. S. Hassanpour, H. Dehghani, A. Z. Snyder, T. Hershey, and J. P. Culver, "Mapping distributed brain function and networks with diffuse optical tomography," *Nature Photonics*, vol. 8, p. 448–454, 2014.

[12] A. Rahmim and H. Zaidi, "Pet versus spect: strengths, limitations and challenges," *Nuclear Medicine Communications*, vol. 29, no. 3, pp. 193–207, 2008.

[13] J. P. Culver, A. M. Siegel, J. J. Stott, and D. A. Boas, "Volumetric diffuse optical tomography of brain activity," *Opt. Lett.*, vol. 28, pp. 2061–2063, Nov 2003.

[14] M. Reisman, M. Z.E., B. A.Q., and C. J.P., "Structured illumination diffuse optical tomography for noninvasive functional neuroimaging in mice," *Neurophotonics*, 2017.

[15] A. Devor, S. Sakadžić, V. J. Srinivasan, M. A. Yaseen, K. Nizar, P. A. Saisan, P. Tian, A. M. Dale, S. A. Vinogradov, M. A. Franceschini, and D. A. Boas, "Frontiers in optical imaging of cerebral blood flow and metabolism," *Journal of Cerebral Blood Flow & Metabolism*, vol. 32, no. 7, pp. 1259–1276, 2012. PMID: 22252238.

[16] A. H. Hielscher, "Optical tomographic imaging of small animals," *Current Opinion in Biotechnology*, vol. 16, no. 1, pp. 79–88, 2005. Analytical biotechnology.

[17] E. Macé, G. Montaldo, I. Cohen, M. Baulac, M. Fink, and M. Tanter, "Functional ultrasound imaging of the brain," *Nature Methods*, vol. 8, p. 662–664, 2011.

[18] T. Deffieux, C. Demene, M. Pernot, and M. Tanter, "Functional ultrasound neuroimaging: a review of the preclinical and clinical state of the art," *Current Opinion in Neurobiology*, vol. 50, pp. 128–135, 2018. Neurotechnologies.

[19] M. Imbault, D. Chauvet, J. Gennisson, and et al., "Intraoperative functional ultrasound imaging of human brain activity," *Scientific Reports*, vol. 7, no. 7304, 2017.

[20] S. Gottschalk, O. Degtyaruk, B. Mc Larney, J. Rebling, M. A. Hutter, X. L. Deán-Ben, S. Shy, and R. Daniel, "Rapid volumetric optoacoustic imaging of neural dynamics across the mouse brain," *Nature Biomedical Engineering*, vol. 3, p. 392–401, 2019.

[21] C. Li, A. Aguirre, J. K. Gamelin, A. Maurudis, Q. Zhu, and L. V. Wang, "Real-time photoacoustic tomography of cortical hemodynamics in small animals," *Journal of Biomedical Optics*, vol. 15, no. 1, pp. 1 – 3, 2010.

[22] J. Yao, J. Xia, K. I. Maslov, M. Nasiriavanaki, V. Tsytsarev, A. V. Demchenko, and L. V. Wang, "Noninvasive photoacoustic computed tomography of mouse brain metabolism in vivo," *NeuroImage*, vol. 64, pp. 257–266, 2013.

[23] X. L. Deán-Ben, S. Gottschalk, B. Mc Larney, S. Shoham, and D. Razansky, "Advanced optoacoustic methods for multiscale imaging of in vivo dynamics," *Chem. Soc. Rev.*, vol. 46, pp. 2158–2198, 2017.

[24] X. L. Deán-Ben, G. Sela, A. Lauri, M. Kneipp, V. Ntziachristos, G. G. Westmeyer, S. Shoham, and D. Razansky, "Functional optoacoustic neuro-tomography for scalable whole-brain monitoring of calcium indicators," *Light: Science & Applications*, vol. 5, 2016.

[25] S. V. Ovsepian, Y. Jiang, T. C. Sardella, J. Malekzadeh-Najafabadi, N. C. Burton, X. Yu, and V. Ntziachristos, "Visualizing cortical response to optoge-

netic stimulation and sensory inputs using multispectral handheld optoacoustic imaging," *Photoacoustics*, vol. 17, p. 100153, 2020.

[26] Y. Ma, M. A. Shaik, S. H. Kim, M. G. Kozberg, D. N. Thibodeaux, H. T. Zhao, H. Yu, and E. M. C. Hillman, "Wide-field optical mapping of neural activity and brain haemodynamics: considerations and novel approaches," *Phil. Trans. R. Soc.*, 2016.

[27] Y. He, M. Wang, X. Chen, R. Pohmann, J. R. Polimeni, K. Scheffler, B. R. Rosen, D. Kleinfeld, and X. Yu, "Ultra-slow single-vessel bold and cbv-based fmri spatiotemporal dynamics and their correlation with neuronal intracellular calcium signals," *Neuron*, vol. 97, 2018.

[28] S. Na, J. J. Russin, L. Lin, X. Yuan, P. Hu, K. B. Jann, L. Yan, K. Maslov, J. Shi, D. J. Wang, L. C. Y., and L. V. Wang, "Massively parallel functional photoacoustic computed tomography of the human brain," *Nature Biomedical Engineering*, 2021.

[29] X. Wang, Y. Pang, G. Ku, X. Xie, G. Stoica, and L. V. Wang, "Noninvasive laser-induced photoacoustic tomography for structural and functional in vivo imaging of the brain," *Nature Biotechnology*, vol. 21, p. 803–806, 2003.

[30] S. Gottschalk, T. F. Fehm, X. L. Deán-Ben, and D. Razansky, "Noninvasive real-time visualization of multiple cerebral hemodynamic parameters in whole mouse brains using five-dimensional optoacoustic tomography," *Journal of Cerebral Blood Flow & Metabolism*, vol. 35, no. 4, pp. 531–535, 2015. PMID: 25586142.

[31] V. Ntziachristos and D. Razansky, "Molecular imaging by means of multispectral optoacoustic tomography (MSOT)," *Chemical Reviews*, vol. 110, no. 5, pp. 2783–2794, 2010.

[32] A. G. Bell, "On the production and reproduction of sound by light," *American Journal of Science*, vol. s3-20, no. 118, pp. 305–324, 1880.

[33] J. J. Rebling, "Rapid Optoacoustic Imaging for Neurology, Cardiology and Vascular Biology," *Doctoral dissertation*, 2019.

[34] F. Helmchen and W. Denk, "Deep tissue two-photon microscopy," *Nature Methods*, vol. 2, no. 12, pp. 932–940, 2005.

[35] A. P. Regensburger, E. Brown, G. Krönke, M. J. Waldner, and F. Knieling, "Optoacoustic imaging in inflammation," *Biomedicines*, vol. 9, no. 5, 2021.

[36] T. L. Szabo, "Chapter 8 - wave scattering and imaging," in *Diagnostic Ultrasound Imaging: Inside Out (Second Edition)* (T. L. Szabo, ed.), pp. 257–294, Boston: Academic Press, second edition ed., 2014.

[37] C. J. H. Ho, N. C. Burton, S. Morscher, U. S. Dinish, J. Reber, V. Ntziachristos, and M. Olivo, *Advances in Optoacoustic Imaging: From Benchside to Clinic*, pp. 75–109. Singapore: Springer Singapore, 2016.

[38] C. Shannon, "Communication in the presence of noise," *Proceedings of the IRE*, vol. 37, pp. 10–21, jan 1949.

[39] A. Özbek, X. L. Deán-Ben, and D. Razansky, "Optoacoustic imaging at kilohertz volumetric frame rates.," *Optica*, vol. 5, pp. 857–863, jul 2018.

[40] M. Xu and L. V. Wang, "Universal back-projection algorithm for photoacoustic computed tomography," *Phys. Rev. E*, vol. 71, p. 016706, Jan 2005.

[41] X. L. Deán-Ben, A. Özbek, and D. Razansky, "Volumetric real-time tracking of peripheral human vasculature with gpu-accelerated three-dimensional optoacoustic tomography," *IEEE Transactions on Medical Imaging*, vol. 32, no. 11, pp. 2050–2055, 2013.

[42] S. Hurand, L.-A. Chauny, H. El-Rabii, S. Joshi, and A. P. Yalin, "Mode coupling and output beam quality of 100–400μm core silica fibers," *Appl. Opt.*, vol. 50, pp. 492–499, Feb 2011.

[43] M. W. Schellenberg and H. K. Hunt, "Hand-held optoacoustic imaging: A review," *Photoacoustics*, vol. 11, pp. 14–27, 2018.

[44] A. E. Siegman, "How to (maybe) measure laser beam quality," in *DPSS (Diode Pumped Solid State) Lasers: Applications and Issues*, p. MQ1, Optical Society of America, 1998.

[45] A. K. Ghatak and K. Thyagarajan, *WKB analysis of multimode fibres*, p. 603–608. Cambridge University Press, 1989.

[46] C. Stacey, R. Jenkins, J. Banerji, and A. Davies, "Demonstration of fundamental mode only propagation in highly multimode fibre for high power edfas," *Optics Communications*, vol. 269, no. 2, pp. 310–314, 2007.

[47] A. E. Ennos, *Speckle Interferometry*, pp. 203–253. Berlin, Heidelberg: Springer Berlin Heidelberg, 1975.